

Three-dimensional numerical simulation of thermocapillary flows in cylindrical liquid bridges

By JENS LEYPOLDT, HENDRIK C. KUHLMANN
AND HANS J. RATH

Center of Applied Space Technology and Microgravity, ZARM, University of Bremen,
Am Fallturm, 28359 Bremen, Germany

(Received 15 July 1998 and in revised form 18 February 2000)

The dynamics of thermocapillary flows in differentially heated cylindrical liquid bridges is investigated numerically using a mixed finite volume/pseudo-spectral method to solve the Navier–Stokes equations in the Boussinesq approximation. For large Prandtl numbers ($Pr = 4$ and 7) and sufficiently high Reynolds numbers, the axisymmetric basic flow is unstable to three-dimensional hydrothermal waves. Finite-amplitude azimuthally standing waves are found to decay to travelling waves. Close to the critical Reynolds number, the former may persist for long times. Representative results are explained by computing the coefficients in the Ginzburg–Landau equations for the nonlinear evolution of these waves for a specific set of parameters. We investigate the nonlinear phenomena characteristic of standing and pure travelling waves, including azimuthal mean flow and time-dependent convective heat transport. For $Pr \ll 1$ the first transition from the two-dimensional basic flow to the three-dimensional stationary flow is inertial in nature. Particular attention is paid to the secondary transition leading to oscillatory three-dimensional flow, and this mechanism is likewise independent of Pr . The spatial and temporal structure of the perturbation flow is analysed in detail and an instability mechanism is proposed based on energy balance calculations and the vorticity distribution.

1. Introduction

Surface tension gradients arise in many physical systems and technical applications in which two immiscible fluids have a common interface. The tangential surface stresses due to the thermocapillary effect can lead to a significant fluid motion commonly called Marangoni convection (see e.g. Kenning 1968 for examples). The relative importance of thermocapillary flows to buoyancy-driven flows which arise simultaneously in crystal growth from a melt was first pointed out by Chang & Wilcox (1975) for the float-zone method (Bohm, Lüdge & Schröder 1994). Today it is well known that the axial micro-segregation (small-scale variations of the concentration) in crystals grown by the float-zone method is mainly caused by oscillatory thermocapillary melt flow.

Since the mid-seventies many experiments on a number of numerical investigations of simple model float-zones have been carried out. In these systems a model liquid is held between two coaxial circular disks, which are kept at different temperatures. This configuration, termed a *half-zone*, is aimed at simulating the upper or lower half of the full liquid zone in the floating-zone crystal-growth process. Owing to the difficulties in measuring the bulk flows in opaque liquids, most of the experiments

used transparent fluids, such as silicone oil, with Prandtl numbers $Pr \geq 1$, much larger than those of liquid metals or semiconductors. Above a critical temperature difference ΔT along the fluid's free surface, or an appropriately defined critical Reynolds number $Re \propto \Delta T$, a transition occurs for high-Prandtl-number fluids directly from the axisymmetric, toroidal, stationary flow to a three-dimensional time-dependent flow (Schwabe & Scharmann 1979; Chun & Wuest 1979). Preisser, Schwabe & Scharmann (1983) measured velocity and temperature profiles and found the relation $m \approx 2.2/\Gamma$ between the azimuthal wavenumber m of the supercritical flow and the aspect ratio $\Gamma = d/R$ of the liquid bridge, where d and R denote the height and radius, respectively. In the oscillatory regime they observed waves travelling in the azimuthal direction. The parameter study by Velten, Schwabe & Scharmann (1991) confirmed the relation found by Preisser *et al.* (1983) and, in addition, provided extensive data on the critical Reynolds numbers and the oscillation frequencies at and above the critical threshold for fluids with Prandtl numbers 1, 7, and 49. Routes into chaos were studied by Frank & Schwabe (1997) for fluids with $Pr = 7, 49$ and 65.

A scaling law for the oscillation frequency in large-Prandtl-number fluids ($Pr \geq 8$), deduced from experiments on the ground and under microgravity, was proposed by Carotenuto *et al.* (1998). An overview on Marangoni flows in crystal growth melts has been given by Schwabe (1988).

One of the first three-dimensional time-dependent simulations of flows in half-zones was carried out by Rupp, Müller & Neumann (1989). For small Prandtl numbers of $O(10^{-2})$ they found that the flow is already three-dimensional below the temperature difference for which it becomes time-dependent. Although using a rather coarse grid, their values for the critical Reynolds numbers for $Pr < 1$ were in order-of-magnitude agreement with estimates from experiments.

Numerical simulations for the same geometry were performed by Savino & Monti (1996) for fluids with $Pr = 30$ and $Pr = 74$. They investigated the influence of a linear time-variation of the Reynolds number on the flow, as used in microgravity experiments, and compared their simulations with experiments done onboard of Maxus 1b (Monti *et al.* 1994) and Spacelab D2 (Monti *et al.* 1995). Moreover, a description of the flow structure for the observed standing and travelling waves with azimuthal wavenumber $m = 1$ was given.

Recently, Levenstam & Amberg (1995) simulated the flow in a half-zone for $Pr = 0.01$ and $Pr = 0$. They found a transition from the axisymmetric basic flow to a three-dimensional stationary flow and, at higher Reynolds numbers, a secondary transition to three-dimensional time-dependent flow. Since the critical Reynolds numbers and the flow patterns did not differ much for both $Pr = 0.01$ and $Pr = 0$, it was concluded that the instabilities at low non-zero Prandtl numbers are hydrodynamic in nature.

Concerning the type of the first instability, their results are in agreement with the linear stability analysis of Wanschura *et al.* (1995), who established the dependence of the critical Reynolds number on the Prandtl number and identified the instability mechanisms for high and low Pr . It was clarified that the hydrothermal wave instability studied experimentally in fluids with $Pr \geq 1$ does not allow conclusions to be drawn for the small-Prandtl-number melts in crystal-growth processes.

The combined effect of buoyancy and thermocapillary forces on the stability of flows in half-zones was investigated by Wanschura, Kuhlmann & Rath (1997). For $Pr = 4$ they found that buoyant forces essentially act to stabilize, the effect being even stronger when the zone is heated from below. Stabilization of the stationary base flow by heating model zones from below rather than from above was also reported by Velten *et al.* (1991).

Despite numerous recent numerical simulations of the full Navier–Stokes equations for the present problem, the results obtained have not been properly placed in the context of bifurcation theory. The present paper thus aims at a thorough analysis of the nonlinear three-dimensional flow in order to elucidate the fundamental properties and mechanisms beyond the first symmetry-breaking instabilities in flows for both small- and large-Prandtl-number liquid bridges. The composition of the supercritical flow is investigated in terms of the amplitudes of the critical mode and its higher spatial harmonics. Characteristic properties of standing and travelling waves in large-Prandtl-number fluids are identified and related to the amplitude equations for the interacting waves. Finally, the time-dependent flow in low-Prandtl-number liquid bridges above the secondary instability is analysed in detail and the mechanism of the instability is discussed.

The paper is arranged as follows. In §2 the problem is formulated in terms of the basic equations and the boundary conditions. Section 3 treats the mathematical and numerical methods used to solve the governing equations. It also addresses the code validation and error estimation. In §4 we present the simulation results the implications of which are discussed in §5.

2. Problem formulation

We consider a liquid bridge supported by surface tension and bounded by two rigid coaxial circular walls of radius R a distance d apart. The liquid is heated from above by keeping the top and bottom walls at constant temperatures $T_0 + \Delta T/2$, and $T_0 - \Delta T/2$, respectively. T_0 is the mean temperature and the aspect ratio is defined as $\Gamma = d/R$. Using the scales d , ν/d , $\rho_0 \nu^2/d^2$, ΔT and d^2/ν for length, velocity, pressure, temperature, and time, where ν and ρ_0 denote the kinematic viscosity and the density of the fluid, the transport equations for momentum and heat in the Boussinesq approximation are

$$(\partial_t + \mathbf{u} \cdot \nabla) \mathbf{u} = -\nabla p + \nabla^2 \mathbf{u} + Gr T \mathbf{e}_z, \quad (2.1)$$

$$(\partial_t + \mathbf{u} \cdot \nabla) T = \frac{1}{Pr} \nabla^2 T, \quad (2.2)$$

$$\nabla \cdot \mathbf{u} = 0. \quad (2.3)$$

Here, $\mathbf{u} = (u, v, w)^T$, p , and T denote the dimensionless velocity, pressure, and temperature fields, and \mathbf{e}_z is the unit vector in the axial direction. The dimensionless parameters are the Prandtl and Grashof numbers, defined as

$$Pr = \frac{\nu}{\kappa}, \quad Gr = \frac{\beta \Delta T g d^3}{\nu^2},$$

where κ is the thermal diffusivity, g the gravitational acceleration, and $\beta = -\rho_0^{-1} (\partial \rho / \partial T)_p$ the thermal expansion coefficient at constant pressure.

On the top and bottom boundaries no-slip and no-penetration conditions are used and constant temperatures are imposed,

$$\mathbf{u} = 0, \quad T = \pm \frac{1}{2} \quad \text{on} \quad z = \pm \frac{1}{2}.$$

On the free surface a linear variation of the surface tension with temperature is assumed, i.e. $\sigma(T) = \sigma_0 - \gamma (T - T_0)$ in dimensional units. Moreover, we consider the limit of asymptotically large mean surface tension σ_0 and a liquid volume of π/Γ^2 . In this limit the liquid bridge takes an upright cylindrical shape which is not influenced

by the static and dynamic pressure and the tangential free-surface stress balance reads

$$\mathbf{S} \cdot \mathbf{n} + Re(\mathbf{I} - \mathbf{nn}) \cdot \nabla T = 0,$$

where $\mathbf{S} = \frac{1}{2}(\nabla \mathbf{u} + (\nabla \mathbf{u})^T)$ is the stress tensor, \mathbf{I} the 3×3 identity, and \mathbf{n} the outward unit normal vector. The normalized strength of the driving shear stress is given by the thermocapillary Reynolds number

$$Re = \frac{\gamma \Delta T d}{\rho_0 v^2}.$$

Heat transfer at the liquid–gas interface is modelled by Newton’s law

$$\partial_r T + Bi(T - T_a) = 0,$$

where, for simplicity, the temperature $T_a = z$ of the ambient gas is assumed to vary linearly with z . The Biot number is defined as

$$Bi = \frac{hd}{\lambda},$$

with h denoting the heat-transfer coefficient and λ the thermal conductivity of the fluid.

On the cylinder’s axis, the relations $\partial_\phi \mathbf{u} = 0$ and $\partial_\phi T = 0$ are used to simplify the volume equation for u at $r = 0$.

3. Numerical techniques and code validation

A finite-volume method on a non-homogeneous staggered grid in the (r, z) -plane combined with a pseudo-spectral approach in the azimuthal direction is used to solve the discretized equations in primitive variables. The standard arrangement of the unknowns is used (u on the $r = \text{const.}$ volume boundaries, w on the $z = \text{const.}$ volume boundaries and v , T and p at the cell centre). Directional gradients of the variables on the boundaries of the two-dimensional control volumes are computed by second-order central differences. On a non-homogeneous grid the accuracy of the central difference discretization formally reduces to first order, but using a moderate grid stretching factor of ≈ 0.95 – 1.05 for neighbouring control volumes, the leading term of the error is comparable in size with the one from the second-order-accurate discretization on a homogeneous grid. For unit aspect ratio the typical resolution used in the (r, z) -plane was $N_r \times N_z = 30 \times 30$ with a cell size reduction for successive control volumes of 0.96 in the radial direction (towards $r = \Gamma^{-1}$) and 0.93 in the axial direction (symmetric from $z = 0$ towards $z = \pm 0.5$).

Since the flow is 2π -periodic in the azimuthal direction, spectral methods are well suited to compute azimuthal derivatives and amplitudes of components with selected azimuthal wavenumbers. Further, for $O(1)$ aspect ratios Γ , the weakly nonlinear three-dimensional flow involves only Fourier modes with low azimuthal harmonics of the fundamental wavenumbers m . Consequently, the flow structure can be resolved to sufficient accuracy with a small number of azimuthal planes, even if higher spatial harmonics are present. Within the pseudo-spectral method employed, the azimuthal derivatives are computed in the Fourier space (Fourier collocation derivatives, Canuto *et al.* 1988). Since no special means have been used to filter out aliasing errors, N_ϕ has to be chosen large enough such that these errors do not change the flow properties. For azimuthal wavenumbers up to $m = 6$, $N_\phi = 14$ azimuthal planes resolved the

Re	1000	3000	5000	7000	Reference
$Pr = 0.02$	8.87	7.18	6.31	5.71	Wanschura
	8.93	7.18	6.31	5.65	This work
$Pr = 4$	2.33	2.05	1.95	1.88	Wanschura
	2.35	2.09	1.97	1.86	This work

TABLE 1. Stream-function minimum $-\min \psi \times 10^3/Re$ for $Pr = 0.02$ and $Pr = 4$ ($Bi = Gr = 0$, $\Gamma = 1$). The results by Wanschura (1998, personal communication) were computed in the stream-function–vorticity formulation using a finite-difference discretization for the z -direction ($N_z = 120$) and a Chebychev-collocation method for the r -direction ($N_r = 30$ modes), while the results for this work were computed on a grid with $N_r \times N_z = 30 \times 30$ volumes.

near-threshold structure to sufficient accuracy, while for the large-Reynolds-number simulations up to $N_\varphi = 26$ was used.

The time stepping is done using an operator-splitting method described in Bristeau, Glowinski & Periaux (1987) (Θ -scheme). One full step consists of three substeps, where in the first and in the last substep the nonlinear terms are treated explicitly, while in the second they are treated fully implicitly. The viscous terms are treated partially implicitly in all substeps. For appropriately chosen substep size and weighting factors of the implicit terms, the scheme can be shown to be second-order accurate in time.

The nonlinear set of equations from the second substep is solved using Newton's iterative method on the linearized system. All linear systems are solved by Stone's strongly implicit procedure (SIP, Stone 1968). Here we have adapted the two-dimensional variant to the block matrix structure resulting from the pseudo-spectral treatment of the azimuthal dependence.

The two- and three-dimensional versions of the code have been validated by comparison with available data for the range of parameters investigated in this work. If not mentioned otherwise, results from linear stability analyses were provided by Wanschura (1998, personal communication) using the method described in Wanschura *et al.* (1995). The following examples are computations for $\Gamma = 1$, $Bi = Gr = 0$.

To assess the accuracy of the (r, z) -discretization, the stream-function minimum of stationary two-dimensional flows is given for $Pr = 0.02$ and $Pr = 4$ for a range of Reynolds numbers. The results are in excellent agreement with those provided by Wanschura (table 1).

To assess the accuracy of the φ -discretization, the growth rate σ and the corresponding oscillation frequency ω of small-amplitude three-dimensional oscillatory perturbations with the critical azimuthal wavenumber $m = m_c$ were determined for Re near Re_c , where Re_c and m_c are the values predicted by the linear stability analysis. To this end, the oscillatory flow was initiated by adding a 2π -periodic ($m = m_c$) perturbation T_p of the temperature field,

$$T_p(r, z, \varphi) = \hat{T} r \Gamma \cos \pi z \sin m \varphi \quad \text{with} \quad \hat{T} = 10^{-3}, \quad (3.1)$$

$$\mathbf{u}_p = 0, \quad (3.2)$$

to the stationary two-dimensional flow. The amplitude of the deviation from the two-dimensional flow either decreased ($Re < Re_c$) or increased ($Re > Re_c$) exponentially in time. Re_c and ω_c were then found by interpolation of σ and ω near the critical point. For the $30 \times 30 \times 14$ mesh used we get $Re_c = 1030$ and $\omega_c = 28.7$, which deviate only

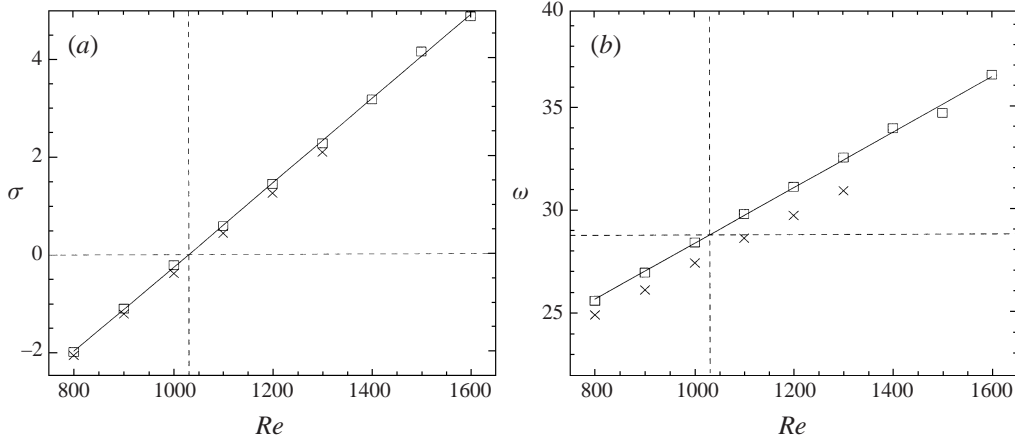


FIGURE 1. (a) Growth rate σ and (b) frequency ω , for $Pr = 4$ and $\Gamma = 1$ as function of Re : \square , simulation; \times , linear stability analysis. Solid line, linear fit to \square .

	v_0	v_2	v_4	v_6	ω
$N_\varphi = 14$	1.48	4.43	1.06	0.289	32.9
$N_\varphi = 22$	1.46	4.39	1.00	0.231	33.1
Difference [%]	1.4	1.0	6.0	25.0	0.6

TABLE 2. Amplitudes of the Fourier modes of the azimuthal velocity v_m at $(r, z) = (0.56, 0.03)$ ($m = 0, 2, 4, 6$) and oscillation frequency for two different azimuthal grids. In both cases $Pr = 4$, $Bi = Gr = 0$, $\Gamma = 1$ and $Re = 1600$; the critical wavenumber is $m_c = 2$ ($N_r \times N_z = 30 \times 30$).

by 2% and 3%, respectively, from the values obtained by the linear stability analysis ($Re_c^{\text{LSA}} = 1047$ and $\omega_c^{\text{LSA}} = 27.9$). The results are presented in figure 1. Starting the simulations from the two-dimensional stationary flow field for $Re > Re_c$ near Re_c with small-amplitude random perturbations, the identical wavenumber m is triggered.

An estimate of the aliasing errors was obtained by comparing the amplitudes of the Fourier components and the oscillation frequency computed with varying azimuthal resolution. For slightly supercritical flow ($Re \approx 1.05 Re_c$) the amplitudes of the basic mode and its higher harmonics as well as the frequencies for both grids are identical. At larger driving forces, $Re \approx 1.50 Re_c$, deviations of order 1% with respect to the total amplitude and also a small shift of the frequency occur. The relative error of single Fourier components, however, may be significantly larger, without influencing the overall properties, e.g. ω (table 2).

The *dynamic* behaviour depends more severely on the grid resolution if $Pr \ll 1$. An interpolation of the growth rate to $\sigma = 0$ still yields the correct (i.e. as given by the linear stability analysis) stability limit, but the values of the exponential growth rate are underestimated by the simulations. On sufficiently fine grids the growth rate reflects the $O(N^{-2})$ accuracy of the discretization (figure 2a), but the linear stability analysis result $\sigma = 7.1$ is only approximately obtained by extrapolating to infinitesimally small grid spacing, which gives $\sigma^\infty = 7.2$. This is in contrast to the accuracy of the two-dimensional flow field, which on a 30×30 mesh is nearly identical with the reference values computed on a 70×70 mesh (figure 2b). Since values of the

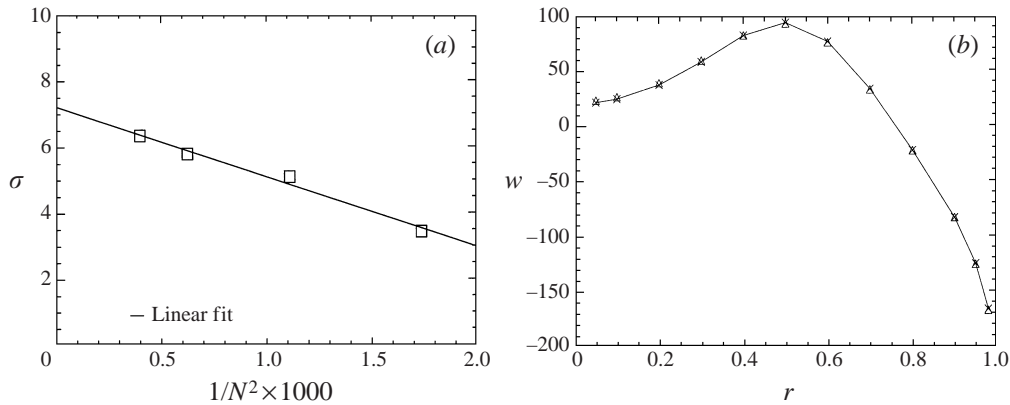


FIGURE 2. (a) Growth rate σ for the small-amplitude three-dimensional flow ($Pr = 0.02$, $Re = 2400$) as a function of grid spacing ($N = N_r = N_z$). (b) Axial velocity $w(r, z = 0)$ on a 30×30 mesh (Δ) and 70×70 mesh (\times).

growth rate for small and zero Prandtl numbers will not be required for the results presented here, all computations were done on a 30×30 mesh.

The adequate representation of the three-dimensional oscillatory flow of low-Prandtl-number fluids demands a high azimuthal resolution. This is due to the larger number of spatial harmonics that must be resolved at high Reynolds numbers and the steep azimuthal velocity gradients that are one source of energy for the oscillatory perturbation (see §4.3.3). Using $N_\phi = 26$ planes, we obtain for $Pr = 0.01$ and $Re = 6500$ an oscillation frequency 5% above the value $\omega = 82$ computed by Levenstam (1994) and reproduce for $Pr = 0$ the critical Reynolds number $Re_c = 5962$ for the onset of oscillations given by Levenstam & Amberg (1995). However, with $N_\phi = 34$ for $Pr = 0$ a positive growth rate of the oscillation amplitude had been found 5% below that value of Re_c . Since the structure of the flow remains qualitatively unchanged and the available CPU time did not allow a higher resolution, all computations reported in this paper were done with $N_\phi = 26$ azimuthal planes. In this case the simulation of one unit of the dimensionless time requires approximately one month of CPU time on a IBM 590 workstation (POWER2 processor at 66 MHz).

4. Results

The hydrothermal wave instability at large Prandtl numbers is considered up to $Pr \leq 7$. High-accuracy calculations for larger Prandtl numbers would require increasingly finer grids to resolve the thermal boundary layers, resulting in excessive CPU times. Although numerous experiments were done with fluids having $Pr > 10$, some of the most reliable data have been obtained for $Pr = 7$ by Velten *et al.* (1991).

4.1. Large Prandtl numbers: $Pr = 4$

For $Pr = 4$ the axisymmetric basic flow becomes unstable to a pair of hydrothermal waves, if $Re > Re_c = 1030$ (§3). At the threshold two solutions, a clockwise and a counter-clockwise travelling wave (TW), bifurcate out of the two-dimensional flow. Within the linear theory, any superposition of both waves with arbitrary amplitudes is possible. To investigate the asymptotic states above threshold, nonlinear calculations for defined initial states were carried out. Throughout §4.1 we consider $\Gamma = 1$ and $Bi = Gr = 0$.

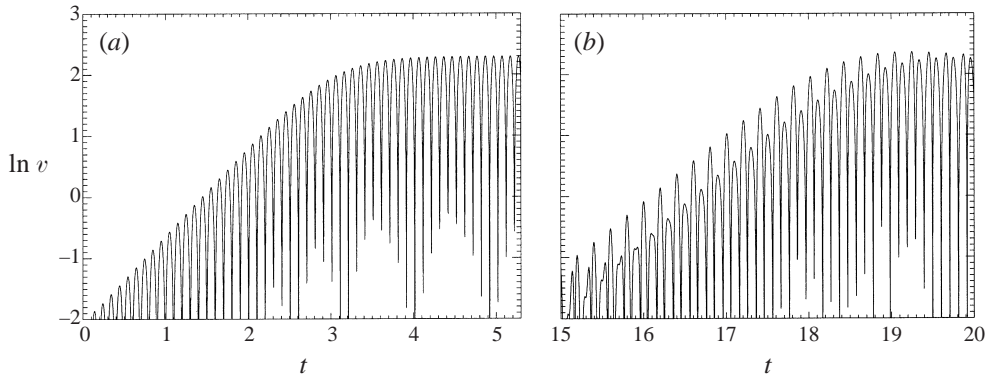


FIGURE 3. Logarithm of the azimuthal velocity as a function of time for $Pr = 4$ and $Re = 1200$. (a) Evolution of the standing wave; $(r, z, \varphi) = (0.95, 0, 0)$. (b) Decay of the standing wave into a travelling wave; $(r, z, \varphi) = (0.95, 0, \pi/4)$.

4.1.1. Stability of standing waves

Standing hydrothermal waves (SWs) of the critical azimuthal wavenumber $m = m_c = 2$ were generated by adding at $t = 0$ the perturbation (3.1) to the two-dimensional stationary flow for the given supercritical Reynolds number. Since the initial perturbation in T does not break the azimuthal reflection symmetry, both the clockwise and the counter-clockwise waves are equally excited and their amplitudes increase at the same rate. Initially, the amplitudes grow exponentially (figure 3a, $t = 0$ –2.5). At a later stage the nonlinear coupling reduces the growth rate ($t = 2.5$ –4.5), before the wave amplitudes finally saturate ($t \approx 4.5$). The location of the SW nodes is arbitrary in principle but in our case it is prescribed by the nodes of the initial temperature perturbation.

Further integration in time, however, shows that standing waves are unstable. At the nodes of the standing wave's azimuthal velocity field the oscillation amplitude can, rather early, be seen to increase exponentially (figure 3b). After a new level of saturation is reached, the flow essentially consists of a travelling wave. Away from the nodes, where the SW has a finite oscillation amplitude, the decay is more difficult to notice.

The scenario is the same for all investigated values of ϵ in the range 0.06–0.54, where the distance from the critical point is defined as

$$\epsilon = \frac{Re - Re_c}{Re_c}.$$

4.1.2. Structure of the hydrothermal waves

Characteristic isolines of the azimuthal velocity and the temperature field are shown in figure 4(a, b) for a standing wave and in figure 4(c, d) for a travelling wave. The axisymmetric part of the corresponding variable, $(1/2\pi) \int x(r, z, \varphi) d\varphi$, has been subtracted to emphasize the three-dimensional structure.†

The full spectral decompositions of the flow for a SW and for a TW are shown in figure 5. The frequency n is given in terms of the fundamental mode's oscillation frequency $\omega \equiv \omega_{m_c}(\epsilon)$, i.e. $|n| = 2$ corresponds to Fourier modes oscillating at $2\omega_{m_c}(\epsilon)$.

† We note that this is not the same as subtracting the two-dimensional base flow, since $(1/2\pi) \int x d\varphi$ includes the axisymmetric contributions generated by nonlinear mode interactions. Therefore, the figures do not show the *complete* perturbations but only their three-dimensional part.

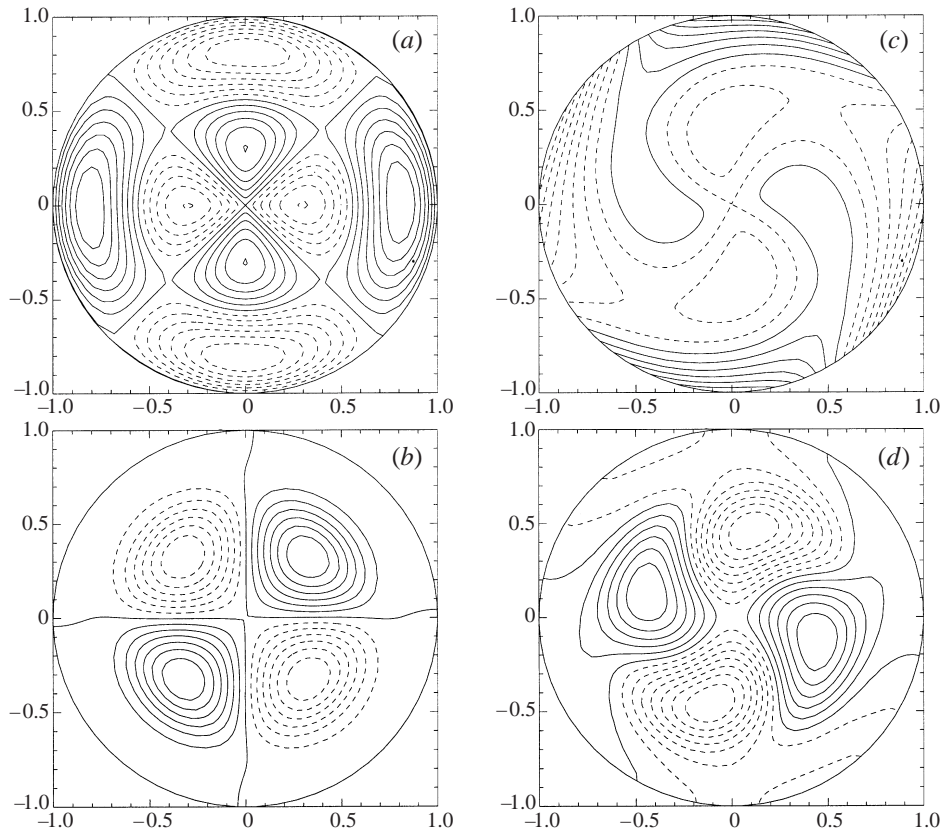


FIGURE 4. (a) Azimuthal velocity and (b) temperature isolines of the standing wave fields, and (c) azimuthal velocity and (d) temperature isolines of the clockwise travelling wave fields at midplane, $z = 0$, for $Pr = 4$, $Re = 1200$. The axisymmetric part has been subtracted and dashed lines correspond to negative values.

We denote by $n > 0$ components propagating clockwise (in the negative φ -direction), and by $n < 0$ components propagating counter-clockwise (in the positive φ -direction). In the following, we shall refer to the flow's Fourier components by u_m^n , v_m^n , etc., where the subscript denotes the azimuthal wavenumber and superscripts specify the temporal harmonics.

A standing wave's spectrum is symmetric with respect to $n = 0$. For the travelling wave the flow consists of a mode with m_c (the fundamental) and its spatial harmonics with the same phase velocity $\omega_m/m = \omega/m_c = \text{const}$.

For the asymptotic states of pure TWs, the amplitudes of the azimuthal velocity of the critical mode and its higher spatial harmonics, v_m , $m = 2, 4$ and 6 , are very well represented by the generic scaling for supercritical bifurcations and quadratic nonlinearity,

$$v_m = \hat{v}_m \epsilon^{m/2m_c}, \quad (4.1)$$

if ϵ is small. Figure 6 shows the amplitudes v_m ($m = 2, 4, 6$) at $(r, z) = (0.5, 0)$ of the azimuthal velocity of the travelling wave as a function of ϵ . They are taken at the approximate location where the v_2 component attains its maximum amplitude in the bulk, but other (r, z) locations or other variables (u , w or T) may be chosen as well. For comparison, lines for $\hat{v}_m \epsilon^{p_m}$ using the coefficients \hat{v}_m and p_m given in table 3 are

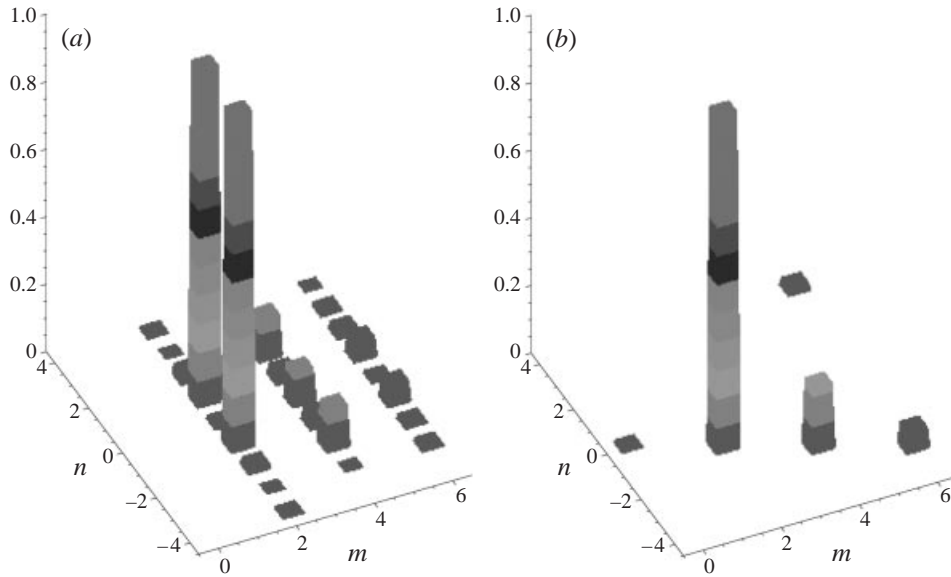


FIGURE 5. Spectral decomposition of the azimuthal velocity at $(r, z) = (0.94, 0)$ for $Pr = 4$, $Re = 1400$. (a) Standing wave ($t \approx 2$), $\omega = 33.7$. (b) Travelling wave ($t \approx 9.25$), $\omega = 31.6$. The contribution to $(m, n) = (6, 4)$ indicates the magnitude of the aliasing error. It originates from the harmonic with $(m, n) = (8, -4)$.

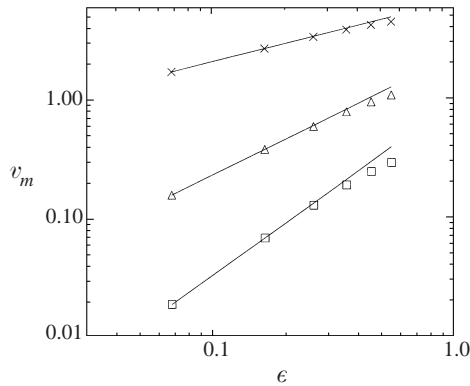


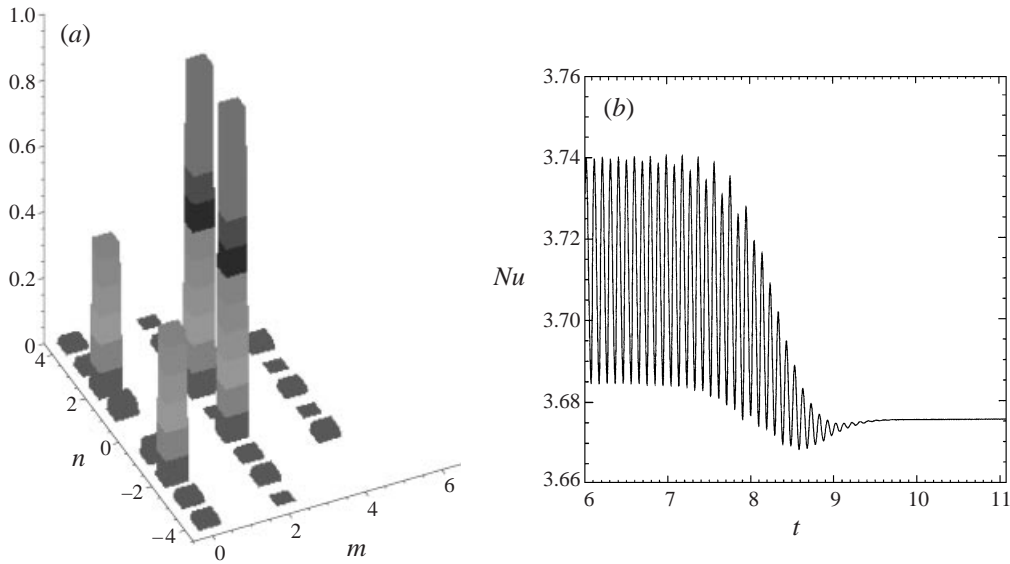
FIGURE 6. Amplitudes v_m of the azimuthal velocity of the travelling wave at $(r, z) = (0.5, 0)$ as a function of ϵ for $m = 2(\times)$, $4(\Delta)$, $6(\square)$ ($Pr = 4$, $Bi = Gr = 0$, $\Gamma = 1$). Solid lines represent the functional dependence $v_m = \hat{v}_m \epsilon^{p_m}$ with the parameters given in table 3.

also shown. The coefficients were obtained using $Re_c = 1030$ (§ 3) and the amplitudes for $Re = 1100$ and $Re = 1200$.

4.1.3. Standing wave properties

For SWs, the coupling of the flow's components $T_{m_c}^{+1}$ and $T_{m_c}^{-1}$ generates components $T_0^{\pm 2}$ oscillating at 2ω (see figure 7, where $m_c = 2$). Due to this component, the integral Nusselt numbers on the top and bottom boundaries are not constant in time, but oscillate at the same frequency, $Nu = \text{const.} + C \sin 2\omega t$. The Nusselt number, which is a measure for the convective heat transport from the top (hot) boundary into the

m	$Pr = 0.02$		$Pr = 4$		$Pr = 7$	
	\hat{v}_m	p_m	\hat{v}_m	p_m	\hat{v}_m	p_m
2	47.41	0.53	6.56	0.50	16.05	0.46
4	21.70	0.98	2.23	0.99	6.04	0.95
6	11.78	1.51	0.93	1.45	3.53	1.46

TABLE 3. Coefficients for the functional dependence $v_m = \hat{v}_m \epsilon^{p_m}$. (See text for details.)FIGURE 7. Coupling of the two counter-propagating waves for $Pr = 4$ and $Re = 1300$. (a) Spectrum of T at $(r, z) = (0.37, 0.49)$ (normalized amplitudes, $\omega = 32.4$). The axisymmetric component at $(m, n) = (0, 0)$ has been dropped. (b) Nusselt number on the top boundary during the decay of the standing wave.

fluid, is defined by $Nu = J/J_c - 1$, where $J = \int \partial_z T|_{z=1/2} r dr d\phi$ and $J_c = \pi/\Gamma^2$. J_c is the heat flux of the purely conductive state.

We evaluated the Nusselt number for the two-dimensional flow, the standing wave regime (in this case the time-averaged value was taken), and the asymptotic state of a travelling wave for different values of $Re > Re_c$. The result is shown in figure 8(a). The Nusselt numbers for all three solutions increase approximately linearly with ϵ and their values for $\epsilon = 0$ agree better than 1% ($Nu_c = 3.42 \pm 0.01$). We find $dNu/d\epsilon = 1.23, 1.09$ and 0.94 for the two-dimensional, SW and TW flows, respectively. For a typical scenario (two-dimensional \rightarrow SW \rightarrow TW) the Nusselt number is decreasing. The asymptotic state of a pure TW has the smallest value of Nu . In figure 8(b) the amplitude of the Nusselt number oscillations in the SW regime is plotted. In the range of ϵ investigated, it is approximately 1% of the time-averaged value of Nu .

For a standing wave there exist azimuthal positions where oscillations of particular Fourier components only can be detected. For any m the SW fields T_m have nodes where the corresponding v_m has anti-nodes, and vice versa. The harmonics of T_m are oriented such that their anti-nodes fall onto the T_m anti-nodes, while the harmonics of v_m are oriented such that their nodes fall onto the v_m nodes.

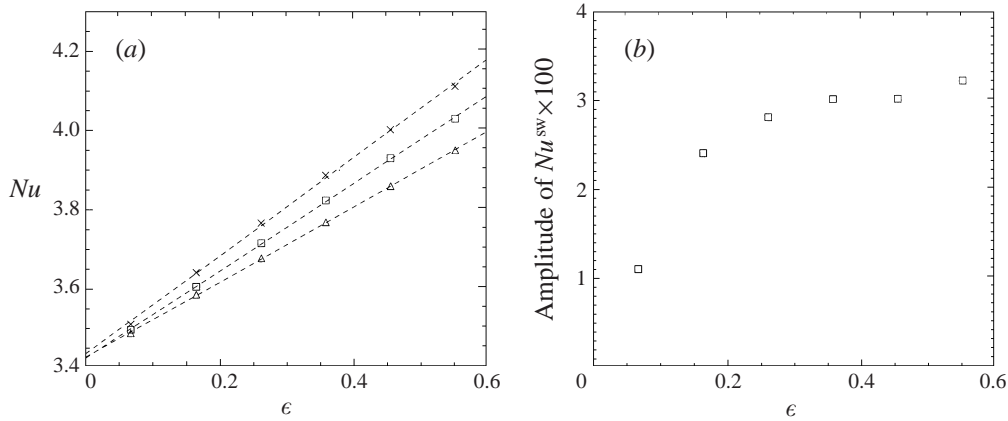


FIGURE 8. Nusselt numbers for $Pr = 4$, $\Gamma = 1$. (a) \times , two-dimensional flow; \square , standing wave (time average); \triangle , travelling wave. (b) Amplitude of the oscillating Nusselt number in the SW regime.

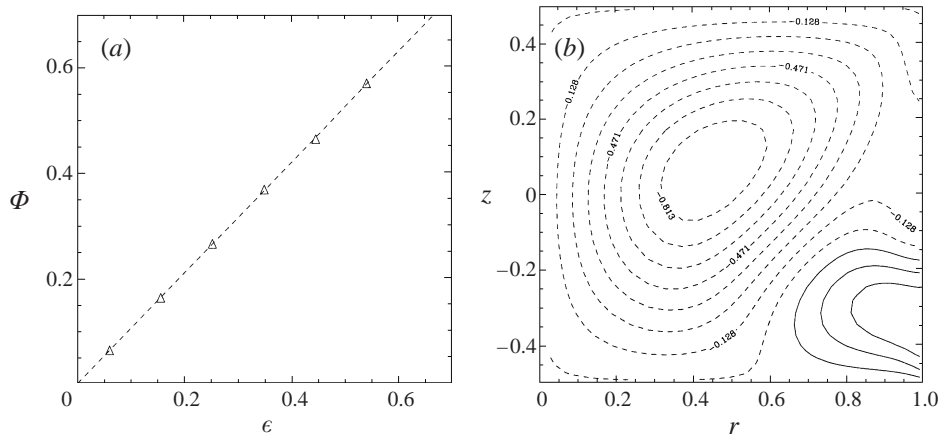


FIGURE 9. Integrated azimuthal flow for $Pr = 4$. (a) Mean flow Φ (\triangle) and linear fit, $Re = 1100$ – 1600 ($Re_c = 1030$). (b) Isolines of v_0^0 for $Re = 1300$. The wave is propagating in the positive φ -direction. Dashed lines correspond to negative values of v_0^0 .

4.1.4. Travelling wave properties

A nonlinear property of TWs is a finite value of the integrated azimuthal flow, defined as

$$\Phi(t) = \frac{1}{2\pi} \int v(r, z, \varphi, t) \, dr dz d\varphi = \int_0^{1/\Gamma} dr \int_{-1/2}^{1/2} dz v_0^0(r, z, t). \quad (4.2)$$

The self-interaction of an azimuthal velocity mode with $m \neq 0$ generates non-zero stationary axisymmetric azimuthal velocity components. Time-dependence is kept in (4.2) to account for transient flow phases. In the asymptotic limit of a pure travelling wave Φ does not depend on time. In figure 9(a) the integrated azimuthal flow for the asymptotic states of pure propagating waves ($Pr = 4$) is shown. It is proportional to ϵ , as $v_2 \propto \sqrt{\epsilon}$ for the supercritical bifurcation (§4.1.5). For the present case we find

$$\Phi = 1.04 \times \epsilon + O(\epsilon^2). \quad (4.3)$$

The mean flow is opposite to the direction of wave propagation. The net value of Φ is the result of a major contribution opposite to the direction of wave propagation (extending over most of the fluid volume) partially compensated by a reverse flow near the cold corner (figure 9b).

Inspecting the convective terms one can easily show that the magnitude and the direction of the mean flow depend on the relative phase shifts with respect to v of the components u and w , which are functions of r and z . Due to symmetry, a *standing* wave has no azimuthal mean flow.

The wave fronts $\varphi_{\pm m}^{\text{wf}}(r, z, t)$ of the clockwise (–) or counter-clockwise (+) travelling wave component with wavenumber m are given by the condition that their phase $\Phi_{\pm m}(r, \varphi, z, t) = \pm m\varphi - \omega_m t + \alpha_m(r, z)$ be constant. We computed $\varphi_{\pm m}^{\text{wf}}$ by a Fourier transform with respect to φ and t of the flow data from one period of oscillation. The curvature of the wave fronts increases with increasing Reynolds number, but the overall shape remains qualitatively unchanged. The phase variation of T along the radial direction causes a large lag between the surface temperature extrema and those in the bulk. This is characteristic for the hydrothermal waves described in Wanschura *et al.* (1995), cf. their figure 18(b), and can also be seen from figure 4(d).

4.1.5. Frequency shift

Nonlinear mode interactions generally modify the oscillation frequencies (see §4.1.6, (4.8) and (4.10)). The frequency right after the generation of the SW perturbation flow, when the three-dimensional amplitudes are still small, is denoted by ω^i and was used to determine ω_c in §3. At the stage when the SW amplitude is saturated, the frequency is ω^{SW} . For $\epsilon < 0.3$, we find $\omega^{\text{SW}} \approx \omega^i$. Finally, for the asymptotic TW we find a third frequency, ω^{TW} . Figure 10 shows that the critical frequencies (28.8, 28.9 and 28.9) extrapolated from ω^i , ω^{SW} and ω^{TW} , respectively, are in agreement within the estimated errors, but the travelling waves' frequency increases with a slope weaker by a factor of 1/2 than that of the standing waves. We find

$$\omega^i = 28.8 + 13.9 \times \epsilon, \quad (4.4)$$

$$\omega^{\text{SW}} = 28.9 + 14.3 \times \epsilon, \quad (4.5)$$

$$\omega^{\text{TW}} = 28.9 + 7.0 \times \epsilon. \quad (4.6)$$

4.1.6. Amplitude equations for hydrothermal waves

Amplitude equations have proven very useful for the description of the weakly nonlinear behaviour (e.g. Newell, Passot & Lega 1993). For the slow time evolution of the complex amplitudes $A_- = Le^{i\alpha_L}$, $A_+ = Re^{i\alpha_R}$ of the fundamental modes of the left- and right-travelling hydrothermal waves the following system of four coupled equations can be derived (see the Appendix):

$$\tau_0 \dot{L} = \epsilon L - g_s L^3 - g_c R^2 L, \quad (4.7)$$

$$\tau_0 \dot{\alpha}_L = c_0 \epsilon - c_2 g_s L^2 - c_3 g_c R^2, \quad (4.8)$$

$$\tau_0 \dot{R} = \epsilon R - g_s R^3 - g_c L^2 R, \quad (4.9)$$

$$\tau_0 \dot{\alpha}_R = c_0 \epsilon - c_2 g_s R^2 - c_3 g_c L^2. \quad (4.10)$$

For stable solutions g_s must be positive (see e.g. Crawford & Knobloch 1991; Iooss 1987). With the scaling $(L, R) \mapsto (L, R)(g_s)^{1/2}$ the coefficient of the cubic self-interaction becomes 1 and $g_c \mapsto \tilde{g}_c = g_c/g_s$ in the above equations. Considering the three cases

τ_0	\tilde{g}_c	c_0	c_2	c_3
0.11	2.29	1.59	0.60	-0.27

TABLE 4. Coefficients in the complex Ginzburg–Landau equations for $Pr = 4$, $\Gamma = 1$, $Gr = 0$, $Bi = 0$.

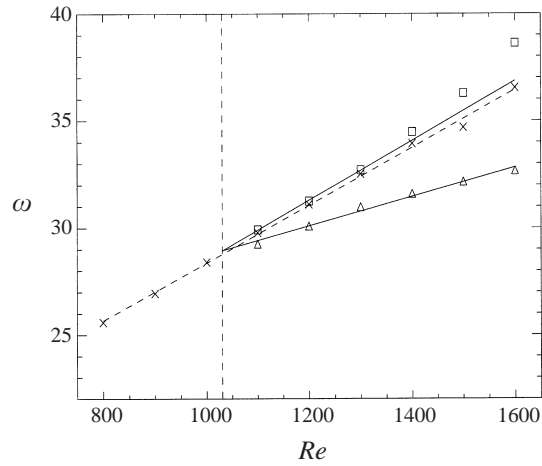


FIGURE 10. Oscillation frequencies for $Pr = 4$, $Bi = Gr = 0$ and $\Gamma = 1$. \times , Initial standing wave ω^i ; \square , fully developed standing wave ω^{SW} ; \triangle , asymptotic travelling wave ω^{TW} . The vertical line marks Re_c .

of small-amplitude exponential growth, saturated nonlinear standing waves ($L = R$), and asymptotic travelling waves (e.g. $L = 0$, $R \neq 0$), it is easy to determine τ_0 , \tilde{g}_c , and c_j ($j = 0, 2, 3$) by fitting the data from the simulations in the weakly nonlinear regime to the appropriate expressions (Appendix). The results for $Pr = 4$, $\Gamma = 1$, $Gr = 0$, and $Bi = 0$ are given in table 4. The sensitivity of the computed coefficient was tested by excluding specific data sets from the fitting procedures. From the resulting scatter the error in the coefficients was estimated to be $\approx \pm 10\%$.

Since $\tilde{g}_c > 1$, the travelling waves are stable while standing waves are not. Considering an asymptotic (left-)travelling wave ($L^2 = \epsilon$, $R = 0$) and using the pair of complex equations given in the Appendix it is easy to show that a small-amplitude counter-propagating wave will decay exponentially $\propto \exp(\sigma_f t)$, where $\sigma_f = (1 - \tilde{g}_c)\epsilon/\tau_0 < 0$ with \tilde{g}_c from table 4. To show the instability of a standing wave with amplitudes $R^2 = L^2 = \epsilon/(1 + \tilde{g}_c)$ for the above parameters, it is sufficient to consider small-amplitude deviations (δ_L, δ_R) from (L, R) , i.e. phase fluctuations need not be taken into account. The analysis of the coupled amplitude equations for δ_L and δ_R yields the growth rates

$$\sigma_{1,2} = \left(\frac{\pm \tilde{g}_c - 1}{\tilde{g}_c + 1} \right) \frac{2\epsilon}{\tau_0}. \quad (4.11)$$

Since $\tilde{g}_c > 1$, there is one positive root σ_1 with corresponding eigenvector $(\delta_L, \delta_R)_1 = (1, -1)\delta$. Hence, initial amplitude differences will grow, leading to the decay of the standing wave. The latter result is confirmed by inspecting the relevant interval in the simulations. From figure 3(b) we find $\sigma_1 = 1.14$ ($\epsilon \approx 0.17$) which compares favourably

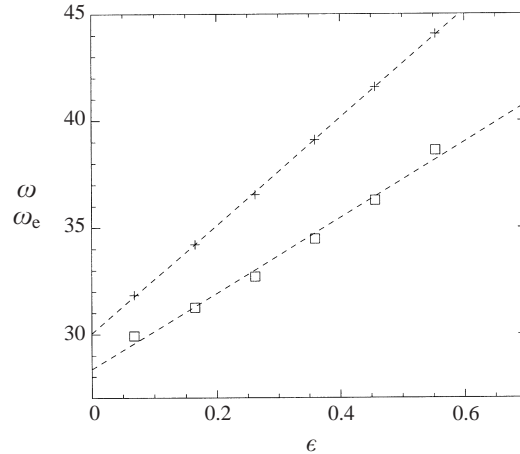


FIGURE 11. Oscillation frequencies ω of the perturbation flow (fully developed SW; \square) and the eddy turnover frequencies ω_e (+) as a function of ϵ for $Pr = 4$, $\Gamma = 1$, $Bi = Gr = 0$. The dashed lines are linear fits to the data.

with $\sigma_1 = 1.13$ predicted by (4.11). Note that although the decay is critically slowed down for $\epsilon \rightarrow 0$, the SWs will decay for all $0 < \epsilon \ll 1$ for the parameters investigated.

4.1.7. Correlation between base state and perturbation flow

Carotenuto *et al.* (1998) have given an empirical correlation for the frequencies of the measured hydrothermal waves. However, the derivation of their formula contains certain ambiguities. A simple physical argument may be based on the fact that the transport of small temperature perturbations in high-Prandtl-number circulating flows is mainly due to advection. The surface temperature fields of the hydrothermal waves in these flows have a spiral character (Muehlner *et al.* 1997) and the iso-surfaces of the perturbation temperature may be imagined as being spirally wrapped around the toroidal basic-state vortex core, m being the winding number. This behaviour becomes more pronounced for higher Pr (Wanschura 1998, personal communication).

If advection were the sole process, the perturbation frequency would correspond to a characteristic eddy turnover frequency ω_e , which can be defined as $\omega_e = 2\pi/T_e$, where

$$T_e = \frac{\pi/\Gamma^2}{\max_z \left\{ \int_{S_+} w dS_+ \right\}}$$

is an estimate for the time it takes the (single) thermocapillary vortex to pump the whole volume of the liquid bridge. Here, S_+ denotes the area for which $w > 0$ at the considered z -level.

The correlation of ω and ω_e should only hold near the critical point, since nonlinear interactions are influencing the frequency (§4.1.5). The comparison shown in figure 11 is better than expected. From the extrapolated values at $Re_c = 1030$ we obtain $\omega_c \approx 0.95\omega_{e,c}$. In fact, larger deviations occur for $Pr = 7$. In this case the correlation at the critical point is $\omega_c \approx 0.81\omega_{e,c}$. Deviations are expected since the basic toroidal vortex is not in rigid body rotation and different streamlines correspond to different periods. Yet, an $O(1)$ agreement of both frequencies is obtained for the Prandtl numbers investigated here.

$\Gamma = d/R$	Bd	LSA m_c	Experiment m	Simulation		
				m	ϵ	Type
0.5	0.282	5	?	5	0.76	TW ⁻
0.6	0.406	4	4	4	0.72	TW ⁺
0.7	0.553	3	3	3	1.19	TW ⁻
0.9	0.914	2 (3)	?	3	0.39	TW ⁻
1.0	1.129	2	2	2	0.51	SW→TW ⁻
1.1	1.366	2	2	2	0.28	TW ⁺
1.3	1.907	2	?	2	0.45	SW→TW ⁺

TABLE 5. Mode types for $\Gamma = 0.5$ – 1.3 , $Pr = 7$, heated from above. Experimental results are taken from figure 14(a) of Velten *et al.* (1991). A question mark indicates that the wavenumber could not be determined satisfactorily. Initial condition for all three-dimensional simulations was the axisymmetric flow at the corresponding Reynolds number. Flow types are shown by SW for standing and TW for travelling (+ clockwise, – counter-clockwise propagation) waves. Arrows indicate a structural change. LSA denotes linear stability analysis.

4.2. Large Prandtl numbers: $Pr = 7$

To compare our simulations with the experiments of Velten *et al.* (1991), the three-dimensional structure of the flow was studied for different values of the aspect ratio Γ at supercritical driving (heated from above). The value used for the Biot number, $Bi = 6.4$, was determined from temperature isolines given in Preisser *et al.* (1983) (their figure 3) for $\Gamma = 1.3$ and was used for all computations. Buoyancy effects were included using a finite Grashof number computed from the fluid properties given in table 1 of Velten *et al.* (1991).

4.2.1. Azimuthal wavenumber selection

For a given aspect ratio the Bond number, $Bd = Gr/Re$, was kept constant in order to account for the fact, that the temperature difference ΔT between top and bottom was varied in the experiments. Table 5 lists the values used in the simulations. For the three-dimensional simulations the axisymmetric flow at the corresponding supercritical Reynolds number was used as initial condition. The azimuthal wavenumbers of the flows that developed out of the *numerical noise* are shown in table 5. With a single exception, these coincide with the azimuthal wavenumbers m_c for Re_c predicted by the linear stability analysis and the azimuthal wavenumbers m determined in the experiments, which, if available, are also given in the table. For $\Gamma = 0.9$ the linear stability analysis predicts $m_c = 2$, while in the simulations at $Re = 1500$ $m = 3$ is found. This is not inconsistent, however, since for this value of the Reynolds number the growth rate for $m = 3$ is larger than for $m = 2$, $\sigma_3 = 4.69 > \sigma_2 = 4.20$. It can be concluded that the simulations correctly predict the azimuthal wavenumber for given aspect ratio also in cases for which experimental data are lacking.

From their experiments Preisser *et al.* (1983) derived the relation

$$m\Gamma = c, \quad (4.12)$$

where $c \approx 2.2$. A least-squares fit to our results implies $c \approx 2.4$, in good agreement with the former.

As for $Pr = 4$, no stable standing waves were found. In two runs SWs were found at onset, but the asymptotic flow in all cases investigated was a pure TW. The waves

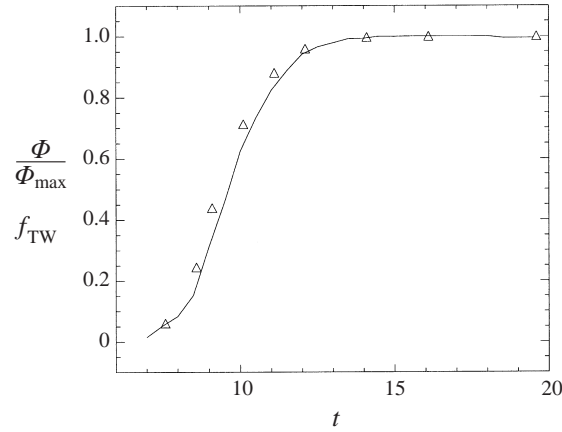


FIGURE 12. Normalized azimuthal net flow Φ (—) and travelling wave fraction f_{TW} (Δ) as a function of time for $Pr = 7$, $Re = 1500$. The lateral size of the symbols approximately represents the period τ used to evaluate the travelling wave fraction.

essentially exhibit the same features as those for $Pr = 4$ and $Gr = 0$ (§4.1), e.g. a time-dependent Nusselt number in the SW regime and a non-zero azimuthal flow in the case of TWs.

For $\Gamma = 1$ the asymptotic flow was investigated for a range of Reynolds numbers. Up to $Re = 1500$ ($\epsilon = 0.51$), the amplitudes v_m , $m = 2, 4$ and 6 , of pure travelling waves approximately follow the scaling law (4.1) for supercritical bifurcations. The coefficients given in table 3 were determined using $Re_c^{\text{LSA}} = 991$ and the amplitudes at $Re = 1200$ and 1300 .

4.2.2. Mixed flow properties

In one of the cases investigated the decay of the standing wave into a travelling wave was slow enough to study the azimuthal mean flow during the transient phase. In figure 12 the normalized value $\Phi(t)$ and the travelling wave fraction f_{TW} are plotted during the decay of the standing wave. The fraction f_{TW} is defined as

$$f_{\text{TW}} = \frac{(v_2^+)^2 - (v_2^-)^2}{(v_2^+)^2 + (v_2^-)^2},$$

where v_2^+ and v_2^- are the amplitudes of the azimuthal velocity at some fixed point (r, z) of the clockwise and counter-clockwise propagating components of the critical mode. While the absolute values of v_2^+ and v_2^- depend on the location (r, z) in the volume, v_2^+/v_2^- and hence f_{TW} are global properties of the mixed flow. For mixed states with finite components v_2^+ and v_2^- the azimuthal mean flow Φ and f_{TW} are approximately proportional to each other.

4.3. Small Prandtl numbers: $Pr \rightarrow 0$

When $Pr \ll 1$ the axisymmetric basic flow first becomes unstable to three-dimensional stationary modes, before a secondary instability leads to oscillatory flow. The purpose of this section is to investigate the secondary instability and its mechanism. All numerical results reported in §4.3 are for simulations with $\Gamma = 1$, $Gr = Bi = 0$.

4.3.1. Three-dimensional stationary flow

In the case $Pr = 0$ the temperature field is purely conductive, i.e. axisymmetric and time-independent. It provides the axial thermocapillary forcing of the flow but decouples from \mathbf{u} . Hence, the instabilities must be due to inertial effects. This is confirmed by the energy transfer analysis of Wanschura *et al.* (1995). Their linear stability analysis of the two-dimensional basic flow with the above parameters gives $Re_c = 1793$ and $m_c = 2$. With increasing Pr azimuthal Marangoni forces counteracting the surface flow of the critical three-dimensional mode stabilize the basic flow (Levenstam & Amberg 1995). An extrapolation of the growth rate $\sigma(Re)$ found in the simulations for $Pr = 0.02$ yields $Re_c^{\text{sim}} = 2108$, which is 2.5% above the linear stability analysis value $Re_c = 2062$. Increasing Re , the amplitudes of the fundamental mode and its harmonics grow according to (4.1), i.e. the instability is also supercritical. For the coefficients given in table 3, $Re_c = 2108$ and the amplitudes at $Re = 2200$ and 2400 were used.

4.3.2. Three-dimensional oscillatory flow

If the Reynolds number is increased further, a secondary instability leads to oscillatory flow. Since the stationary basic flow is not homogeneous in φ , the perturbation eigenmode may be represented by a series of coupled Fourier modes. From the linearized perturbation equations for a stationary base state with fundamental wavenumber $m_0 > 0$ it is easy to show that the system of Fourier modes decouples into m_0 independent sets of equations, within each of which the Fourier modes are separated by m_0 :

$$S_l = \{m | m = l + \mu m_0, \mu \in \mathbb{N}\}, \quad l = 0, 1, \dots, m_0 - 1. \quad (4.13)$$

In the present case we have $m_0 = m_c = 2$. Therefore two types of oscillatory perturbation modes exist. In general both neutral oscillatory modes have different critical Reynolds numbers. One mode consists of harmonics with odd wavenumbers ($m = 1, 3, 5, \dots$), the other one has even wavenumbers ($m = 0, 2, 4, \dots$) only.

In the present simulations the former type, composed of odd Fourier modes, is realized. Figure 13 shows the spectral decomposition of the time-dependent flow for $Re = 6000$ (slightly above the onset of oscillations) and for $Re = 7200$. The components with $n = 0$ constitute the stationary base flow. It consists of the fundamental mode with $m = 2$ and its spatial harmonics. The components with $n = \pm 1$ and odd wavenumbers m represent the time-dependent perturbation. Close to the onset of the oscillations, the variation is almost harmonic in time. If the Reynolds number is increased, contributions with $n = \pm 2, \pm 3 \dots$ appear, making the oscillations increasingly anharmonic. In the (m, n) -plane, the non-zero components are arranged in a checkerboard manner. The components with frequencies n and $-n$ were observed to approach equal amplitudes in the asymptotic state, i.e. the perturbation is a *stable standing wave*. Close to the critical threshold, where the higher temporal harmonics ($|n| > 1$) are small compared to the components with $n = \pm 1$, the squared amplitudes of the latter grow proportional to $\epsilon = Re/Re_{c2} - 1$,

$$(v_m^{\pm 1})^2 \propto \epsilon, \quad m = 1, 3, \dots,$$

i.e. the bifurcation is supercritical. The critical Reynolds numbers for the secondary instability were obtained by extrapolating the squared oscillation amplitude to zero. We find $Re_{c2} = 5960$, $\omega_{c2} = 80$ for $Pr = 0$ and $Re_{c2} = 7160$, $\omega_{c2} = 93$ for $Pr = 0.02$.

The value of Re_{c2} for $Pr = 0$ is nearly identical with that given by Levenstam

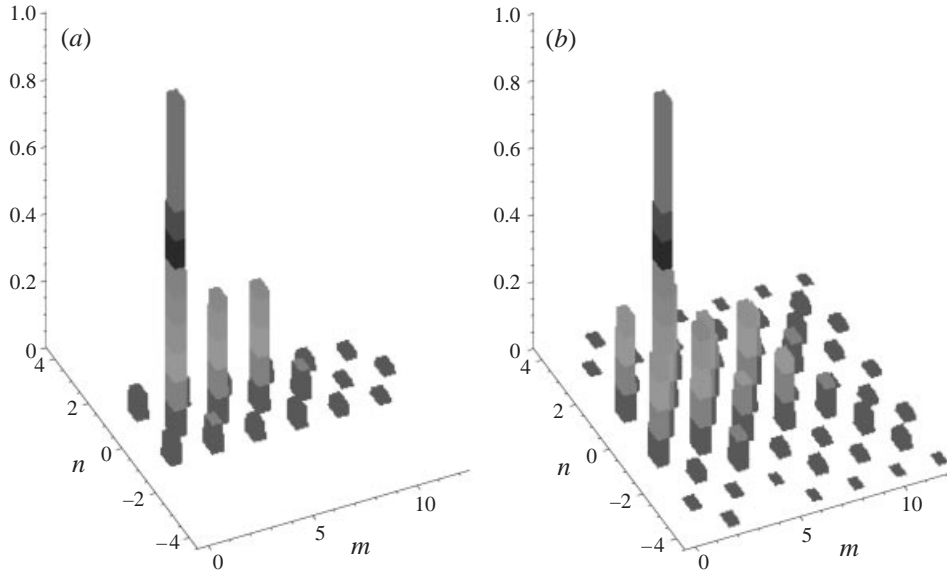


FIGURE 13. Spectral composition of the flow computed from $v(t)$ at $(r, z) = (0.7, -0.2)$ for $Re = 6000$ (a) and $Re = 7200$ (b). The peak amplitudes correspond to $v_2^0 = 22.0$ and 27.4 , respectively.

& Amberg (1995). Our simulations confirm their description of the oscillatory flow and also that the same type of instability occurs for $Pr = 0$ and $Pr = O(10^{-2})$, indicating that the mechanism is independent of the temperature field. In view of this the following detailed analysis of the three-dimensional time-dependent flows is restricted to the zero-Prandtl-number limit.

4.3.3. Energy transfer analysis

To elucidate the mechanism of the instability the energy transfer between the stationary basic flow and the perturbation flow is analysed. For this purpose we write the total flow \mathbf{u} as a sum of the stationary base flow \mathbf{u}_0 and the time-dependent perturbation \mathbf{u}_1 ,

$$\mathbf{u}(\mathbf{r}, t) = \mathbf{u}_0(\mathbf{r}) + \mathbf{u}_1(\mathbf{r}, t).$$

Inserting \mathbf{u} into the Navier–Stokes equations, linearizing with respect to \mathbf{u}_1 , multiplying by \mathbf{u}_1 and integrating over the fluid volume yields the Reynolds–Orr equation for the perturbation which, for our boundary conditions, reads

$$\partial_t E_{\text{kin}} = \int \mathbf{u}_1 \cdot (\nabla^2 \mathbf{u}_1) dV - \int \mathbf{u}_1 \cdot (\mathbf{u}_1 \cdot \nabla \mathbf{u}_0) dV = -D + \sum_{i=0}^9 I_i, \quad (4.14)$$

where D is the rate of dissipation and the integrals I_i ($i = 0, 1, \dots, 9$) denote the work per unit time done by the Reynolds stresses on the base flow. The work done by azimuthal and axial Marangoni forces vanishes for $Pr \rightarrow 0$.

The stationary base flow \mathbf{u}_0 was computed by averaging N (usually $N = 16$) flow fields sampled at equally spaced time intervals $\Delta t = \tau/N$. An evaluation of the integrals in the Reynolds–Orr equation for one complete period of the oscillations is shown in figure 14. There are four terms that provide the main energy for the

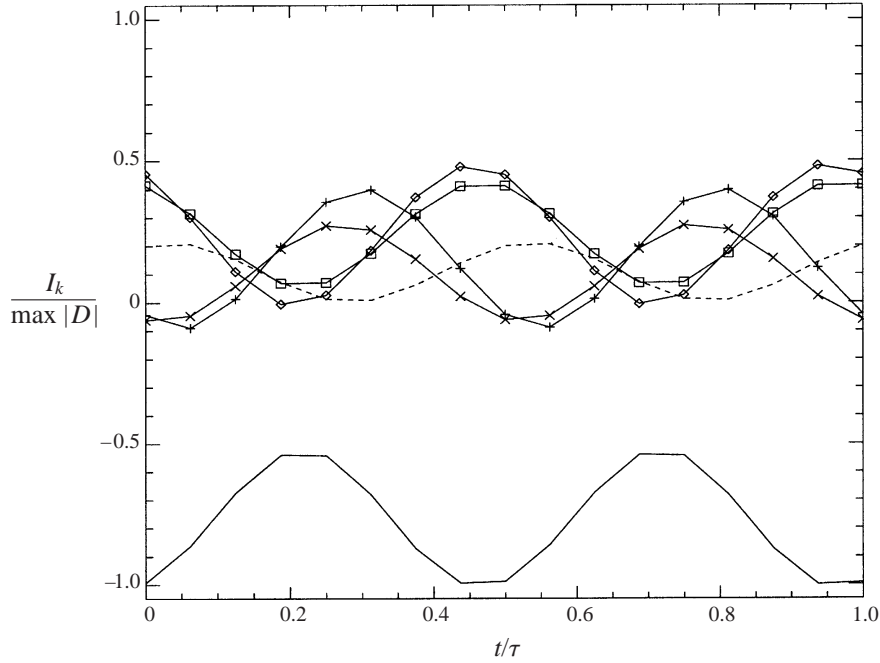


FIGURE 14. Most relevant integrals in the Reynolds–Orr equation as a function of time for $Re = 6000$. All terms are normalized with respect to the maximum of $|D|$. $-D$ (—), I_1 (\square), I_2 ($+$), I_5 (\times), I_7 (\diamond), I_9 (---). The contribution of the integrals not shown is less than that indicated by I_9 .

perturbation flow, namely

$$I_1 = - \int u_1^2 \partial_r u_0 \, dV, \quad I_7 = - \int w_1 u_1 \partial_r w_0 \, dV, \quad (4.15)$$

$$I_2 = - \int \frac{u_1 v_1}{r} \partial_\phi u_0 \, dV, \quad I_5 = - \int \frac{v_1^2}{r} \partial_\phi v_0 \, dV. \quad (4.16)$$

All Reynolds-stress terms have also been analysed locally to exclude the cases where large contributions in one part of the volume are compensated by large contributions with opposite sign in other parts, which would result in small but nevertheless important integrals. It turns out that integrals other than the above have minor contributions throughout the fluid volume.

The perturbation flow gains its energy alternately from azimuthal base-state velocity gradients (I_2 , I_5) and from radial base-state gradients (I_1 , I_7). The integral maxima of the latter two terms are delayed by $\Delta t \approx 0.15 \tau$ with respect to those of the former two. Figure 15 shows the local distribution of their integrands, weighted with the corresponding control volume size dV . Note that the term I_7 also provides the energy for the first (stationary) instability (Wanschura *et al.* 1995).

4.3.4. Time evolution of the perturbation flow

Horizontal cuts of the perturbation flow indicate that it is localized near the vertical plane along $\phi = 0, \pi$ (figure 16a). For the visualization of the vortical structures in the oscillatory flow we employ the method of Jeong & Hussain (1995) who considered the tensor $\Pi = \mathbf{S}^2 + \mathbf{Q}^2$, where $S_{ij} = \frac{1}{2}(\partial_i u_j + \partial_j u_i)$ and $Q_{ij} = \frac{1}{2}(\partial_i u_j - \partial_j u_i)$ are the symmetric and the anti-symmetric part of the velocity-gradient tensor, respectively.

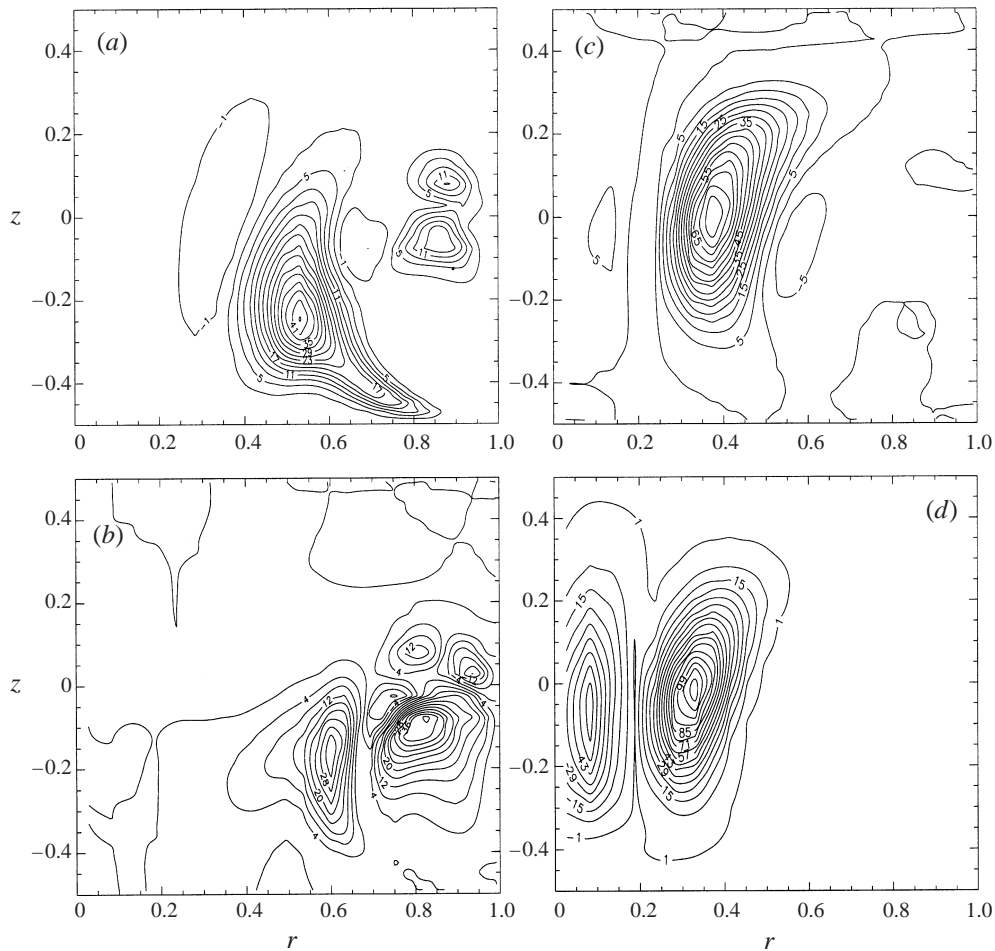


FIGURE 15. Local distribution of the terms I_1 (a), I_7 (b), I_2 (c) and I_5 (d) in the plane $\varphi = -\pi/26$ for $Re = 6000$. All terms are shown for the time when they attain their maximum integral contribution (cf. figure 14).

The tensor Π approximately corresponds to $-\nabla\nabla p$ but does not contain transient and viscous effects. If the eigenvalues are ordered such that $\zeta_1 \leq \zeta_2 \leq \zeta_3$, the vortex core is identified as the region in which Π has two negative eigenvalues ζ_i , i.e. where $\zeta_2 < 0$. By this method, structures of weak vorticity can also be clearly visualized.

The vortex structures in the perturbation flow are illustrated in figure 17 by a sequence of isoline-plots of ζ_2 during half a period of the oscillations. The structures correspond to cigar-like regions of nearly axial vorticity, as can be seen from figure 16(b).

In figure 17(a) two fully developed vortex pairs 1 and 2 are seen. As time proceeds both inner vortices (pair 1) are annihilated and are replaced by the two fragments 2a that split from the outer pair (b). During the temporary increase of vorticity of the new inner pair (c,d), the remainders 2b and 2c disappear and a new vortex pair 3 is generated closely above them (c). This new pair has opposite vorticity to the former pair 2 and the fragments 3b will take its role in the second half of the oscillation period.

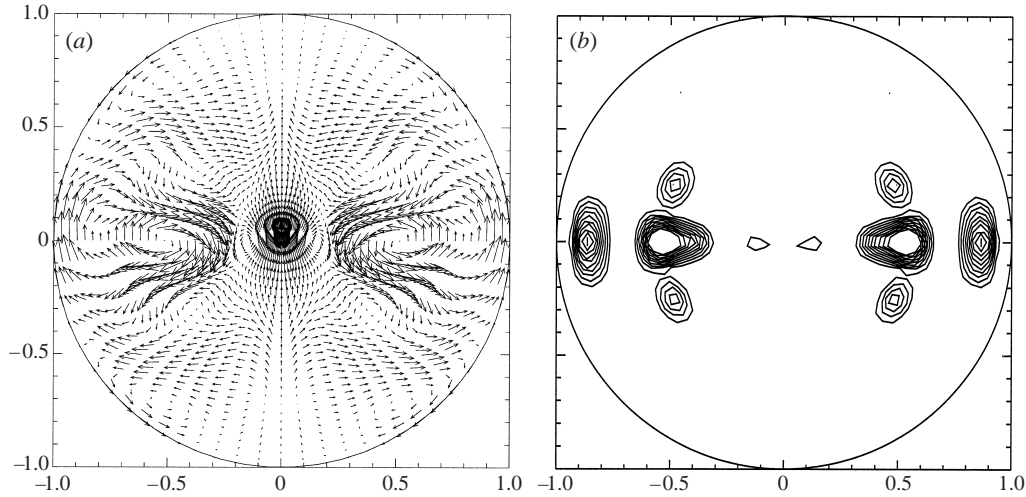


FIGURE 16. Horizontal cuts of the *perturbation* flow at $z = -0.15$ for $t/\tau = \frac{7}{16}$ ($Re = 6000$, $Pr = 0$). (a) Velocity field, (b) isolines of ζ_2 . The instant corresponds to figure 17(b).

Depending on the phase of the oscillation and the respective position of a vortex pair, its vortices are driven alternately by the two mechanisms associated with $I_{1,7}$ and $I_{2,5}$ before annihilation near $r = 0$. Comparing figures 14 and 17 shows that the process associated with the integrals I_2 and I_5 drives both the inner and the outer vortices around $t/\tau \approx \frac{1}{4}$. When the vorticity of the inner pair is decaying, the outer pair is driven by the energy from I_1 and I_7 . During phases of maximum energy supply from these terms, two fragments split from the outer pair and replace the inner two vortices.

4.3.5. Mechanism of the secondary instability

While there is no obvious reason for the oscillatory nature of the supercritical flow, the vortical structures that appear can, at least, be compared with those known for much simpler geometries and base flows. To draw this parallel, we note that with increasing Reynolds number the saddle-shaped steady three-dimensional basic toroid is stretched out when its core is displaced radially outward at the two opposite sides ($\varphi = 0$ and $\varphi = \pi$ in the figures shown) and pulled into the cold (bottom) corner, while at $\pi/2$ relative to these ($\varphi = \pi/2$ and $\varphi = 3\pi/2$) it is shifted towards the hot (upper) boundary and towards the cylinder's axis of symmetry. In this qualitative description the location of the vortex is identified as the point $(r(\varphi), z(\varphi))$ where $u(r, z) = w(r, z) = 0$. This is illustrated in figure 18(c, d).

During this process the cold boundary stagnation point near $(r, z) = (0, -0.5)$ present for *axisymmetric* flow develops into a so-called unstable node at $z = -0.25$ on the cylinder's axis. Parts of the fluid approaching this point from $\varphi = \pi/2$ and $3\pi/2$ form an upward-directed straining flow, but others are pushed radially outwards at $\varphi = 0$ and π , as can be seen in the horizontal cut of figure 18(a, b). The strong deflection of the latter parts generates the large azimuthal gradients which are the source of the energy production mechanism represented by the integrals (4.16), I_2 and I_5 . When meeting with the backflow of the thermocapillary vortex near $r = 0.6$ the outward streams give rise to two more regions of straining flow (figures 18a and 18c), where large radial gradients favour the energy production by the integrals (4.15), I_1 and I_7 . Initially inclined (vortices 3b in figure 17 d), the vortices generated hereby are

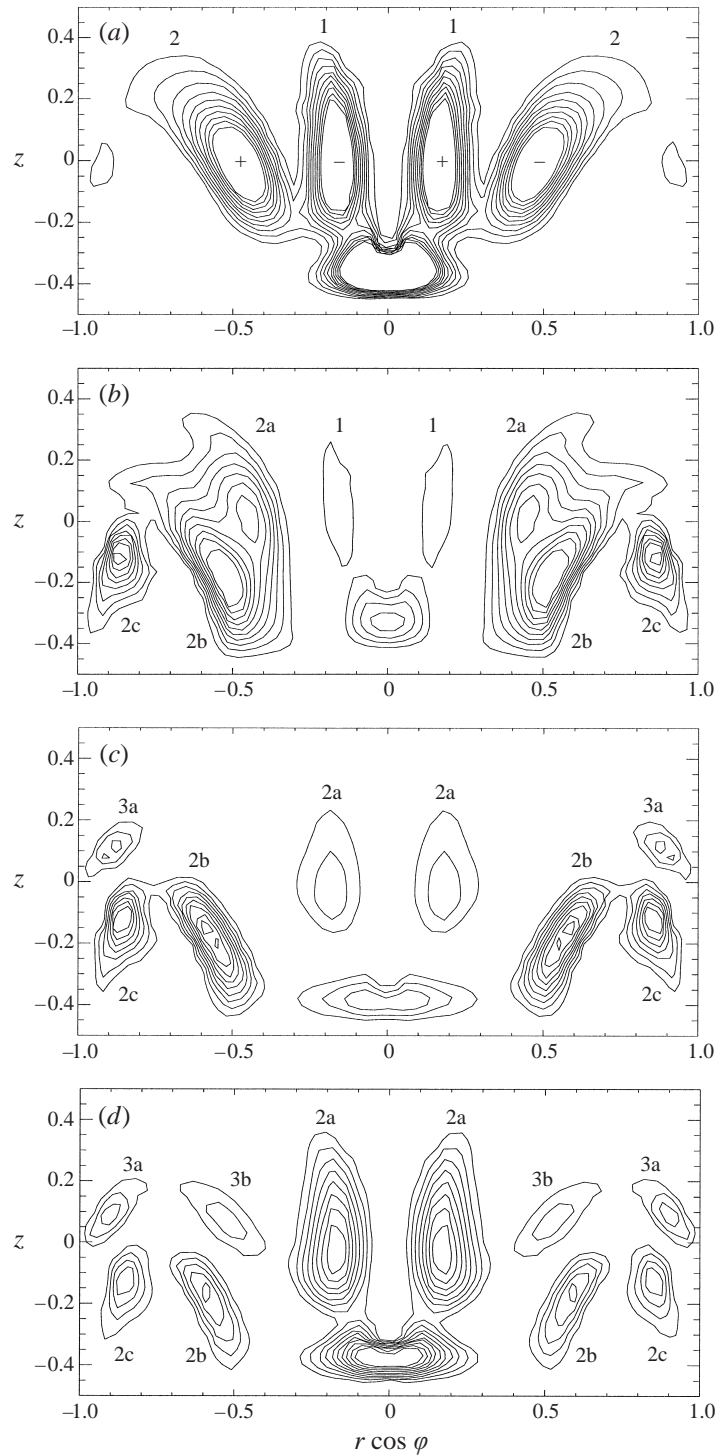


FIGURE 17. Time evolution of the vortex structures of the perturbation at $Re = 6000$ in the plane $\varphi = 0, \pi$. Isolines of ζ_2 are shown for (a) $t/\tau = \frac{1}{4}$, (b) $\frac{7}{16}$, (c) $\frac{9}{16}$, and (d) $\frac{10}{16}$ (τ : period of oscillation). Neighbouring vortices have opposite vorticity as indicated in (a). Isolines below $\zeta_{\min} = -100$ are not shown, causing the plateaus inside strong vortices.

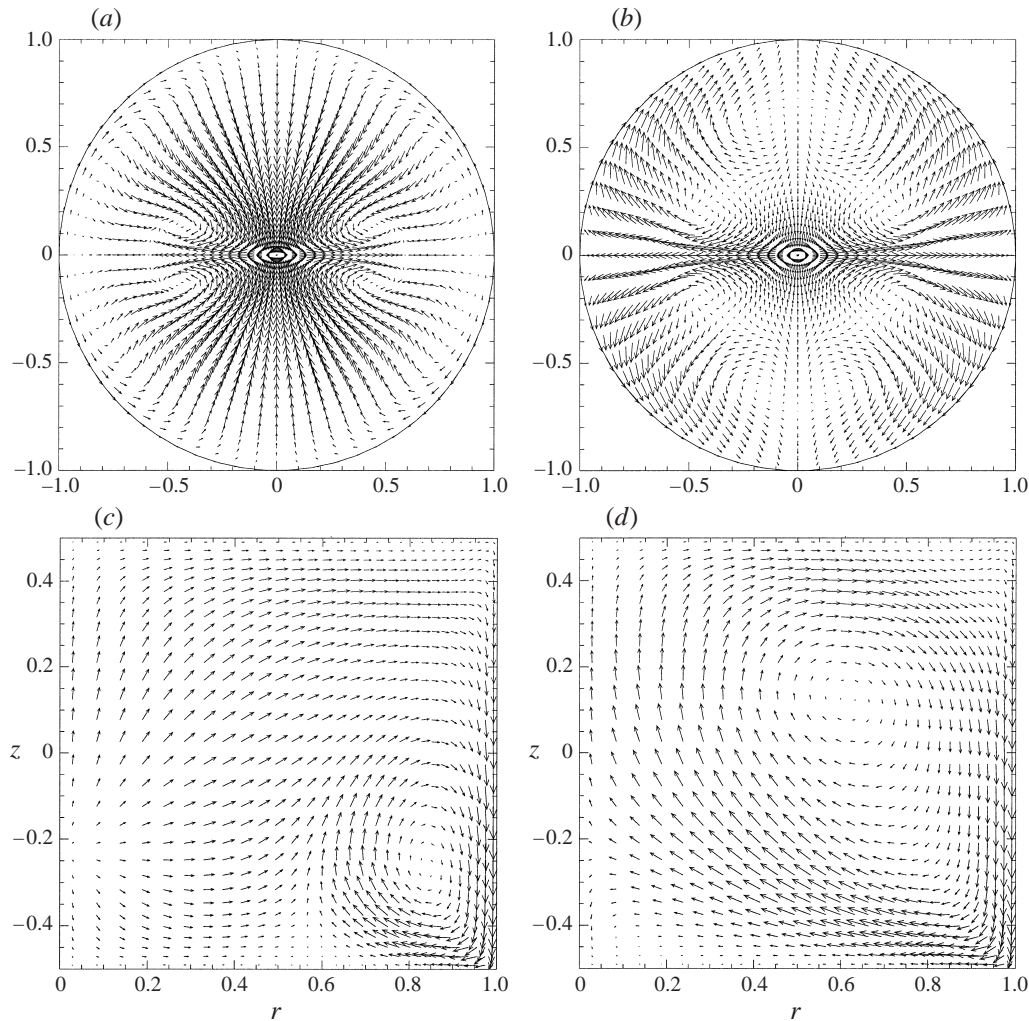


FIGURE 18. Stationary base flow for $Re = 6000$ projected onto the planes (a) $z = -0.30$, (b) $z = 0.10$, (c) $\varphi = 0$, (d) $\varphi = \pi/2$.

aligned upward along the direction of the central straining flow of the basic state during their evolution (vortices 1 and 2a in figure 17a–c).

Most hyperbolic stagnation point flows are unstable (Lagnado, Phan-Thien & Leal 1984; Kerr & Dold 1994). The unstable modes typically consist of vortices with vorticity aligned in the principle strain direction amplified by vortex stretching. Since the regions of energy production identified above for the half-zone have stagnation point flow character and since the straining motion associated herewith obviously enforces an alignment of the perturbation vorticity, we conclude that the instability is due to the same mechanism (compare figures 17 and 18c, d).

The secondary structures in the linear flows studied by Kerr & Dold (1994) are steady. In the present case the secondary flow is oscillatory, which may be related to the lack of translational invariance perpendicular to the respective planes of main strain, but also to the coupling of the two regions where vortices are generated with the central straining flow. Note that the locations of the inner vortices are approximately

($r \approx 0.2, \varphi = 0, \pi$). It is essentially their strength, and not their position, that oscillates in time.

5. Discussion and conclusions

Thermocapillary flows in differentially heated cylindrical liquid bridges for both small (0 and 0.02) and large Prandtl numbers (4 and 7) have been investigated. Results from linear stability analyses were confirmed throughout. Simulations above the stability limit of the axisymmetric stationary basic state were used to investigate typical nonlinear properties of these flows, e.g. interactions of propagating hydrothermal waves (stability of SWs, mean flow, time-dependent heat transfer), and the instability of the three-dimensional stationary flow in low-Prandtl-number fluids.

5.1. Large Prandtl numbers

For fluids with $Pr = O(1)$ the two-dimensional axisymmetric basic flow becomes unstable to hydrothermal waves. Using appropriate initial conditions, standing waves, i.e. flows with counter-propagating waves of equal amplitude, can be generated initially. For all parameters investigated mixed waves, however, are found to be unstable and the asymptotic state is a pure travelling wave containing only components which propagate in the same direction. This is consistent with the observations of Preisser *et al.* (1983) for a fluid of $Pr = 8.9$. For zones with fluids of $Pr = 1$ and $Pr = 7$ heated from above Velten *et al.* (1991) also identified azimuthally travelling waves for most of the parameters investigated.

Standing and travelling waves ($Pr = 30$ and $74, \Gamma = 2$ and $3, m = 1$) also have been observed by Savino & Monti (1996). They found standing waves to appear during a time interval right after the onset of oscillatory flow. The successive evolution into a travelling wave was attributed to the large amplitudes of the perturbation, which continued to grow during the standing wave state in their calculations. This is different to our findings, where travelling waves are the asymptotic states for *all* investigated values of ϵ , i.e. even for small-amplitude perturbations. For $\epsilon \rightarrow 0$, however, the decay of the standing wave is critically slowed down, as is seen from σ_1 in (4.11), and requires asymptotically long simulation runs to be detected.

We anticipate that this critical slowing down is also responsible for an untypical case reported by Castagnolo & Carotenuto (1999) for a unit-aspect-ratio liquid bridge and $Pr = 1$. In a simulation with Re only $\approx 0.5\%$ above Re_c the authors were not able to observe the decay of the standing wave prior to the end of the calculation at $t \approx 50$. However, as can be seen from their figure 5(a), the oscillation amplitude of the temperature signal was still increasing, indicating that the asymptotic state has not been reached yet. The asymptotic states found in runs with higher Re or for $Pr = 32$ (aspect ratio 1 and 2) were travelling waves.

Nonlinear equilibrium states of obliquely travelling waves in thin liquid layers with a temperature gradient imposed on the free surface have been studied by Smith (1988). By a multiple scales analysis he derived a set of generalized Ginzburg–Landau equations for the coupled waves which is similar to (A 1)–(A 2) but includes slow spatial amplitude variations. For a thermally insulated free surface travelling waves are stable for all Prandtl numbers, while for $Bi = 1$ and $Pr \leq 0.01$ standing waves are stable. This is in full analogy with our present results for $Pr = 4$ and $Bi = 0$.

The travelling waves studied for $Pr = 4$ and 7 exhibit a finite azimuthal mean flow opposite to the direction of wave propagation. Presumably, this is the cause of the azimuthal transport of tracer particles in a NaNO_3 ($Pr = 7$) float-zone of aspect

ratio $\Gamma = 0.25$ reported recently by Schwabe, Hintz & Frank (1996). For $Re \approx 2Re_c$ they observed groups of tracer particles, which were trapped in the centre of the thermocapillary vortex, moving azimuthally back and forth in an *asymmetric* manner, such that there was a net movement of the particles in the direction of propagation of the travelling wave. This, however, does not contradict our result of the *net* flow being opposite to the wave propagation. For large Prandtl numbers and small aspect ratio Γ the centre of the thermocapillary vortex may well be in the region of co-propagation of the azimuthal flow (cf. the lower right in figure 9b). In fact this is found to be the case for $\Gamma = 0.5$, the smallest aspect ratio investigated in our simulations for $Pr = 7$. The mean flow velocity at the vortex centre for $Re = 2100 \approx 1.75Re_c$ is $\approx 1^\circ \text{ s}^{-1}$ (for NaNO_3), in qualitative agreement with the experimental value of $\approx 1.5^\circ \text{ s}^{-1}$ (figure 10 in Schwabe *et al.* 1996).

In general, the wave fronts $\varphi_{\pm}^{\text{wf}}(r, z)$ of the waves, i.e. the surfaces of constant phase $\Phi_{\pm} = \pm m\varphi - \omega t + \alpha(r, z) = \text{const.}$, are not planar. At a given location (r, φ, z) this is equivalent to a wave propagating with a local wave vector

$$\mathbf{k}_{\pm} = \nabla \Phi_{\pm} = \left(\frac{\partial \alpha}{\partial r}, \pm \frac{m}{r}, \frac{\partial \alpha}{\partial z} \right)^{\text{T}}.$$

For a standing wave, in particular, only the radial and axial wave-vector components remain (Kuhlmann & Rath 1993).

In the cases investigated ($Pr = 4$ and $Pr = 7$) we do not find a strong corkscrew-like twisting of the wave fronts at $r = 1/\Gamma$, as was reported by Muehlner *et al.* (1997) for an experiment with a fluid of $Pr = 35$. Close to Re_c the wave fronts of the component with $m = m_c$ are dominating the supercritical flow. For example, in the case of $Pr = 4$ and $\epsilon = 0.46$ the temperature wave front's head and tail on the cylinder's surface have a phase difference $\Delta\varphi_{\pm 2; \text{s}}^{\text{wf}} = 9^\circ$, whereas the maximum phase difference in the plane (r, z) is $\Delta\varphi_{\pm 2; \text{max}}^{\text{wf}} = 70^\circ$. In the case of $Pr = 7$, $\epsilon = 0.51$, the corresponding values are $\Delta\varphi_{\pm 2; \text{s}}^{\text{wf}} = 11^\circ$ and $\Delta\varphi_{\pm 2; \text{max}}^{\text{wf}} = 121^\circ$. Hence, at least near the outer surface, the twist of the wave fronts is weak. Muehlner *et al.* (1997) observed a uni-directional tilting of the wave front on the surface with $k_z = \partial_z \alpha > 0$, i.e. the waves seem to travel upstream with respect to the basic surface flow (as do the hydrothermal waves investigated by Smith 1988). For the cited simulations this also holds true near $z = 0$, whereas close to the rigid walls intervals with $k_z < 0$ also exist. Hydrothermal waves in an infinite liquid column subject to an axial surface temperature gradient have been studied by Xu & Davis (1984). They find that for $O(1)$ Prandtl numbers the critical mode has $m = 1$ and travels downstream.

The wavenumber m selected in the weakly nonlinear regime is proportional to the inverse of the aspect ratio Γ of the system. This is consistent with the observations of Preisser *et al.* (1983) and Velten *et al.* (1990) (see also Kuhlmann 1999) and the linear-stability analysis of Wanschura *et al.* (1995) for $Pr \ll 1$.

5.2. Small Prandtl numbers

For fluids with $Pr \ll 1$ the two-dimensional axisymmetric flow first becomes unstable to a three-dimensional stationary perturbation. On increasing the Reynolds number a secondary instability leads to an oscillatory flow in form of a stable standing wave. The critical mode has odd spectral content (Fourier modes with $m = 1, 3, 5, \dots$). Its temporal harmonics oscillating at $|n|\omega$ ($|n| > 1$) alternately have even and odd spectral content, leading to a checkerboard-like structure in the (m, n) -plane of figure 13.

Since $m = 2$ for the stationary three-dimensional basic flow, there also exists a perturbation mode which, close to its corresponding threshold, consists of components with *even* wavenumbers only. The instability is of odd type, i.e. spatially subharmonic to the driving basic flow with $m_c = 2$. (This is similar to the subharmonic resonance found in other nonlinear forced systems, e.g. the Mathieu oscillator.) Hence we conclude that the even-wavenumber eigenmode must have a growth rate smaller than that of the odd-wavenumber mode for the parameters investigated.

We confirm the results of Wanschura *et al.* (1995) (regarding the first instability) and Levenstam & Amberg (1995) that the instabilities are inertial for $Pr = 0$ and for small non-zero Prandtl numbers. The energy transfer analysis shows that the energy for the time-dependent perturbation flow is generated in the bulk rather than on the surface. The relevant terms involve radial and azimuthal gradients of the three-dimensional stationary base flow. A characteristic feature of the perturbation flow is the alternating growth and decay of two pairs of nearly straight, counter-rotating vortices. Their axes are oriented parallel to the main axis (e_z) of the straining flow generated by the three-dimensional base flow near $r = 0$. The similarities with linear stagnation point flows suggests that the vortex stretching in this region is the origin of the instability and that the observed orientation is caused by vorticity alignment in the straining flow.

Critical Reynolds numbers for full-zone configurations under normal gravity have been calculated by Kaiser & Benz (1998). Even though $Bd = 0.5$, they find that thermocapillary convection is dominating. For cylindrical zones with $\Gamma = 1.5$ they obtain $3500 < Re_{c2} < 4500$. This is consistent with our results, if we assume that the increased dissipation in a half-zone owing to the hot rigid boundary must be compensated by a larger driving. The critical Reynolds number for the onset of oscillatory flow was determined experimentally by Cröll *et al.* (1991). They used a heated zone with partially covered surface and found $Re_{c2} = 7000 \pm 2000$.

These results support the relevance of the half-zone system for the modelling of flows in full floating zones. We note, however, that for real floating zone configurations Γ is such that for the first (stationary) instability $m_c = 1$ is expected, eventually modifying details of the secondary instability's mechanism. At least, we may conclude from §4.3.2 that the oscillatory mode includes all wavenumbers ($m = 0, 1, 2, \dots$).

We are very grateful to M. Wanschura for providing the linear stability data. This work was partially supported by DLR under grant number 50 WM 9443.

Appendix. Amplitude equations for travelling waves

We consider the travelling wave instability of a stationary base state that is translation-invariant in the spatial dimension denoted by x . Close to the onset the spatially periodic perturbation can be written in terms of the left- and right-travelling waves,

$$A(x, t) = A_L(x, t)e^{i(kx + \omega t)} + A_R(x, t)e^{i(kx - \omega t)} + \text{c.c.}$$

For the slow temporal and spatial modulation of A_L and A_R two coupled complex Ginzburg–Landau (CGL) equations hold, which in the general form are (Cross 1988)

$$\begin{aligned} \tau_0(\partial_t + v\partial_x)A_R &= \epsilon(1 + ic_0)A_R + (1 + ic_1)\xi_0^2\partial_x^2 A_R \\ &\quad - g_s(1 + ic_2)|A_R|^2 A_R - g_c(1 + ic_3)|A_L|^2 A_R, \end{aligned} \quad (\text{A } 1)$$

$$\begin{aligned} \tau_0(\partial_t - v\partial_x)A_L &= \epsilon(1 + ic_0)A_L + (1 + ic_1)\xi_0^2\partial_x^2 A_L \\ &\quad - g_s(1 + ic_2)|A_L|^2 A_L - g_c(1 + ic_3)|A_R|^2 A_L. \end{aligned} \quad (\text{A } 2)$$

Here, i denotes the imaginary unit, $i = \sqrt{-1}$, v is the group velocity and τ_0 , ξ_0 , g_s , g_c , and c_j ($j = 0, 1, 2, 3$) are real coefficients. In the case of the hydrothermal wave instability in a cylindrical liquid bridge the coordinate x corresponds to $r\varphi$ and the corresponding wavenumber k equals m/r . For $\Gamma = O(1)$ the system admits small integer wavenumbers m only and slightly above the critical Reynolds number only $m = m_c$ and its harmonics are present. Consequently there is no slow spatial modulation of the amplitude,

$$\begin{aligned} A_L(\varphi, t) &\equiv A_L(t) = L(t)e^{iz_L(t)}, \\ A_R(\varphi, t) &\equiv A_R(t) = R(t)e^{iz_R(t)}. \end{aligned}$$

Insertion into the CGL equations and separating real and imaginary parts, we obtain the four coupled differential equations (4.7)–(4.10).

The coefficient τ_0 is determined from the exponential growth rate σ when the amplitude of the perturbation flow is far from its saturated value. Then only terms linear in L and R need to be considered, which gives

$$L(t), R(t) \propto e^{\epsilon t/\tau_0}.$$

Thus, $\tau_0 = \epsilon/\sigma$. The value of τ_0 given in table 4 was computed by a linear least-squares fit of $\sigma(\epsilon)$.

For a standing wave with saturated amplitude, i.e. $L = R$ and $\dot{L} = \dot{R} = 0$. We obtain

$$L^2 = R^2 = \frac{\epsilon}{g_s + g_c} \quad \mapsto \quad \frac{\epsilon}{1 + \tilde{g}_c}, \quad (\text{A } 3)$$

$$\tau_0\dot{\alpha}_L = \tau_0\dot{\alpha}_R = \left(c_0 - \frac{c_2 + c_3 g_c/g_s}{1 + g_c/g_s}\right)\epsilon \quad \mapsto \quad \left(c_0 - \frac{c_2 + c_3 \tilde{g}_c}{1 + \tilde{g}_c}\right)\epsilon, \quad (\text{A } 4)$$

where the right-hand-side expressions result from rescaling the amplitudes according to $L^2/g_s \mapsto L^2$ and $R^2/g_s \mapsto R^2$. Then g_s and g_c in (4.7)–(4.10) are replaced by 1 and $\tilde{g}_c = g_c/g_s$, respectively. For an asymptotic, say, pure left-travelling wave $R = \dot{R} = \dot{L} = 0$ and

$$L^2 = \frac{\epsilon}{g_s} \quad \mapsto \quad \epsilon, \quad (\text{A } 5)$$

$$\tau_0\dot{\alpha}_L = (c_0 - c_2)\epsilon \quad (\text{A } 6)$$

The values for g_s and g_c were derived as the linear coefficients from least-squares fits of the squared amplitudes of saturated standing and asymptotic travelling waves $v_{2,SW}^2(\epsilon)$ and $v_{2,TW}^2(\epsilon)$ as a *quadratic* function of ϵ . The quadratic term was retained to account for a weak curvature of the data. The frequency shift observed for initial and saturated standing as well as travelling waves (§4.1.4) is caused by $\dot{\alpha}$. If the wave amplitudes are of $O(\epsilon)$, the terms $\propto L^2, R^2$ in (4.8) and (4.10) can be omitted and c_0 is obtained from

$$\tau_0\dot{\alpha}_{L,R} = c_0\epsilon.$$

Finally, c_2 and c_3 are calculated from (A 4) and (A 6). We computed c_0 , c_2 , and c_3 from linear least-squares fits of the appropriate oscillation frequencies as a function of ϵ .

REFERENCES

- BOHM, J., LÜDGE, A. & SCHRÖDER, W. 1994 Crystal growth by floating zone melting. In *Handbook of Crystal Growth 2a, Basic Techniques* (ed. D. T. J. Hurle), pp. 213–257. North Holland.
- BRISTEAU, M. O., GLOWINSKI, R. & PERIAUX, J. 1987 Numerical methods for the Navier–Stokes equations. Application to the simulation of compressible and incompressible viscous flows. *Comput. Phys. Rep.* **6**, 73–187.
- CANUTO, C., HUSSAINI, M. Y., QUARTERONI, A. & ZHANG, T. A. 1988 *Spectral Methods in Fluid Dynamics*. Springer.
- CAROTENUTO, L., CASTAGNOLO, D., ALBANESE, C. & MONTI, R. 1998 Instability of thermocapillary convection in liquid bridges. *Phys. Fluids* **10**, 555–565.
- CASTAGNOLO, D. & CAROTENUTO, L. 1999 Numerical simulation of three-dimensional thermocapillary flows in liquid bridges. *Numer. Heat Transfer A* **36**, 859–877.
- CHANG, C. E. & WILCOX, W. R. 1975 Inhomogeneities due to thermocapillary flow in floating zone melting. *J. Cryst. Growth* **28**, 8–12.
- CHUN, C.-H. & WUEST, W. 1979 Experiments on the transition from steady to oscillatory Marangoni convection in a floating zone under reduced gravity effect. *Acta Astronautica* **6**, 1073–1082.
- CRAWFORD, J. D. & KNOBLOCH, E. 1991 Symmetry and symmetry-breaking bifurcations in fluid dynamics. *Ann. Rev. Fluid Mech.* **23**, 341–387.
- CRÖLL, A., MÜLLER-SEBERT, W., BENZ, K. W. & NITSCHKE, R. 1991 Natural and thermocapillary convection in partially confined silicon melt zones. *Microgravity Sci. Technol.* **3**, 204–215.
- CROSS, M. C. 1988 Structure of nonlinear travelling-wave states in finite geometries. *Phys. Rev. A* **38**, 3593–3600.
- FRANK, S. & SCHWABE, D. 1997 Temporal and spatial elements of thermocapillary convection in floating zones. *Exps. Fluids* **23**, 234–251.
- FU, B.-I. & OSTRACH, S. 1985 Numerical solutions of thermocapillary flows in floating zones. In *Transport Phenomena in Materials Processing*, pp. 1–9. ASME.
- IOOSS, G. 1987 Reduction of the dynamics of a bifurcation problem using normal forms and symmetries. In *Instabilities and Nonequilibrium Structures* (ed. E. Tirapegui & D. Villarroel), pp. 3–40. D. Reidel.
- JEONG, J. & HUSSAIN, F. 1995 On the identification of a vortex. *J. Fluid Mech.* **285**, 69–94.
- KAISER, TH. & BENZ, K. W. 1998 Floating-zone growth of silicon in magnetic fields; III. Numerical simulation. *J. Cryst. Growth* **183**, 564–572.
- KENNING, D. B. R. 1968 Two-phase flow with nonuniform surface tension. *Appl. Mech. Rev.* **21**, 1101–1111.
- KERR, O. S. & DOLD, J. W. 1994 Periodic steady vortices in a stagnation point flow. *J. Fluid Mech.* **276**, 307–325.
- KUHLMANN, H. C. 1994 Thermocapillary flows in finite size systems. *Math. Comp. Modelling* **20**, 145–173.
- KUHLMANN, H. C. 1999 *Thermocapillary Convection in Models of Crystal Growth*. Springer.
- KUHLMANN, H. C. & RATH, H. J. 1993 On the interpretation of phase measurements of oscillatory thermocapillary convection in liquid bridges. *Phys. Fluids A* **5**, 2117–2120.
- LAGNADO, R. R., PHAN-THIEN, N. & LEAL, L. G. 1984 The stability of two-dimensional linear flows. *Phys. Fluids* **27**, 1094–1101.
- LEVENSTAM, M. 1994 Thermocapillary convection in floatzones. PhD thesis, Department of Mechanics, Stockholm, Sweden.
- LEVENSTAM, M. & AMBERG, G. 1995 Hydrodynamical instabilities of thermocapillary flow in a half-zone. *J. Fluid Mech.* **297**, 357–372.
- MONTI, R., ALBANESE, C., CAROTENUTO, L., CASTAGNOLO, D. & CEGLIA, E. 1995 First results from the Onset experiment during Spacelab mission D-2. *Scientific Results of the German Spacelab Mission D-2*, pp. 247–258.
- MONTI, R., FORTEZZA, R., CASTAGNOLO, D. & DESIDERS, D. 1994 The Telemaxus experiment on oscillatory Marangoni flow. ESA SP 1132, vol. 4, pp. 44–59.
- MUEHLNER, K. A., SCHATZ, M. F., PETROV, V., MCCORMICK, W. D., SWIFT, J. B. & SWINNEY, H. L. 1997 Observation of helical traveling-wave convection in a liquid bridge. *Phys. Fluids* **9**, 1850–1852.

- NEWELL, A. C., PASSOT, T. & LEGA, J. 1993 Order parameter equations for patterns. *Ann. Rev. Fluid Mech.* **25**, 399–453.
- PREISSER, F., SCHWABE, D. & SCHARMANN, A. 1983 Steady and oscillatory thermocapillary convection in liquid columns with free cylindrical surface. *J. Fluid Mech.* **126**, 545–567.
- RUPP, R., MÜLLER, G. & NEUMANN, G. 1989 Three-dimensional time dependent modelling of the Marangoni convection in zone melting configurations for GaAs. *J. Cryst. Growth* **97**, 34–41.
- SAVINO, R. & MONTI, R. 1996 Oscillatory Marangoni convection in cylindrical liquid bridges. *Phys. Fluids* **8**, 2906–2922.
- SCHWABE, D. 1988 Surface-tension-driven flows in crystal growth melts. *Crystals* **11**, 75–114.
- SCHWABE, D., HINTZ, P. & FRANK, S. 1996 New features of thermocapillary convection in floating zones revealed by tracer particle accumulation structures (PAS). *Microgravity Sci. Technol.* **9**, 163–168.
- SCHWABE, D. & SCHARMANN, A. 1979 Some evidence for the existence and magnitude of a critical Marangoni number for the onset of oscillatory flows in crystal growth melts. *J. Cryst. Growth* **46**, 125–131.
- SHEN, Y. 1989 Energy stability of thermocapillary convection in a model of float-zone crystal growth. PhD thesis, Arizona State University.
- SMITH, M. K. 1988 The nonlinear stability of dynamic thermocapillary liquid layers. *J. Fluid Mech.* **194**, 391–415.
- STONE, H. L. 1968 Iterative solution of implicit approximations of multidimensional partial differential equations. *SIAM J. Num. Anal.* **5**, 530–558.
- VELTEN, R., SCHWABE, D. & SCHARMANN, A. 1991 The periodic instability of thermocapillary convection in cylindrical liquid bridges. *Phys. Fluids A* **3**, 267–279.
- WANSCHURA, M., KUHLMANN, H. C. & RATH, H. J. 1997 Linear stability of two-dimensional combined buoyant-thermocapillary flow in cylindrical liquid bridges. *Phys. Rev. E* **55**, 7036–7042.
- WANSCHURA, M., SHEVTSOVA, V. M., KUHLMANN, H. C. & RATH, H. J. 1995 Convective instability mechanisms in thermocapillary liquid bridges. *Phys. Fluids* **7**, 912–925.
- XU, J.-J. & DAVIS, S. H. 1984 Convective thermocapillary instabilities in liquid bridges. *Phys. Fluids* **27**, 1102–1107.